Journal of Organometallic Chemistry 694 (2009) 1529–1541

Contents lists available at ScienceDirect

Journal of Organometallic Chemistry

journal homepage: www.elsevier.com/locate/jorganchem

Long-distance electronic interaction in a molecular wire consisting of a ferrocenyl–ethynyl unit bridging two [(η^5-C_5H_5)(dppe)M] metal centers

Teng-Yuan Dong *, Shu-Fan Lin, Chiao-Pei Chen, Shu-Wen Yeh, Hsing-Yin Chen, Yuh-Sheng Wen

Department of Chemistry, National Sun Yat-Sen University, Kaohsiung 804, Taiwan
Faculty of Medicinal and Applied Chemistry, Kaohsiung Medical University, Kaohsiung 804, Taiwan
Institute of Chemistry, Academia Sinica, Nankang, Taipei, Taiwan

ARTICLE INFO

Article history:
Received 19 November 2008
Received in revised form 19 December 2008
Accepted 24 December 2008
Available online 3 January 2009

Keywords:
Molecular wire
Redox systems
Alkynyl ligands
Ferrocene
Bridging ligands

ABSTRACT

Several multinuclear ferrocenyl–ethynyl complexes of formula [(η^5-C_5H_5)(dppe)M^{II}–C≡C–(fc)$_n$–C≡C–M^{II}(dppe)(η^5-C_5H_5)] (fc = ferrocenyl; dppe = $Ph_2PCH_2CH_2PPh_2$; **1**: M^{II} = Ru^{2+}, n = 1; **2**: M^{II} = Ru^{2+}, n = 2; **3**: M^{II} = Ru^{2+}, n = 3; **4**: M^{II} = Fe^{2+}, n = 2; **5**: M^{II} = Fe^{2+}, n = 3) were studied. Structural determinations of **2** and **4** confirm the ferrocenyl group directly linked to the ethynyl linkage which is linked to the pseudo-octahedral [(η^5-C_5H_5)(dppe)M] metal center. Complexes of **1**–**5** undergo sequential reversible oxidation events from 0.0 V to 1.0 V referred to the Ag/AgCl electrode in anhydrous CH_2Cl_2 solution and the low-potential waves have been assigned to the end-capped metallic centers. The *solid-state* and *solution-state* electronic configurations in the resulting oxidation products of **[1]**$^+$ and **[2]**$^{2+}$ were characterized by IR, X-band EPR spectroscopy, and UV–Vis at room temperature and 77 K. In **[1]**$^+$ and **[2]**$^{2+}$, broad intervalence transition band near 1600 nm is assigned to the intervalence transition involving photo-induced electron transfer between the Ru^{3+} and Fe^{2+} metal centers, indicating the existence of strong metal-to-metal interaction. Application of Hush's theoretical analysis of intervalence transition band to determine the nature and magnitude of the electronic coupling between the metal sites in complexes **[1]**$^+$ and **[2]**$^{2+}$ is also reported. Computational calculations reveal that the ferrocenyl–ethynyl-based orbitals do mix significantly with the (η^5-C_5H_5)(dppe)Ru metallic orbitals. It clearly appears from this work that the ferrocenyl–ethynyl spacers strongly contribute in propagating electron delocalization.

1. Introduction

The insight provided by the rich chemistry of bridged mixed-valence binuclear complexes has promoted a great deal of both experimental and theoretical studies. Considerable work has been focused on the use of mixed-valence complexes to probe electronic coupling between well-separated metal sites [1–3]. Recently, the study of homo- and hetero-metallic binuclear transition metal complexes in which the end-capped metal centers are connected by π-conjugated organic linear spacers has been an intriguing area of research, since such system may provide the possibility to study the electronic coupling between the redox-active end-capped metal centers, or propose as models for molecular wires. In this context, end-capping of unsaturated organic spacers with various redox-active groups, such as ferrocene, ruthenium(II) polypyridine [4–9], [RuL_2Cl] (L_2 = $2PPh_3$, $Ph_2PCH_2CH_2PPh_2$ (dppe)) [10,11], and [M(η^5-C_5H_5)L_2] (M = Fe(II), Ru(II), and Os(II)) metal centers [12–21], have been most studied where they are intended to promote the long-range electronic coupling. The nature of the end-capped metal center and π-conjugated organic spacer plays significantly important role in determining the magnitude of electronic coupling. The magnitude of electrochemical data $\Delta E_{1/2}$ has been taken as an indication of the magnitude of electronic coupling between two redox metal centers, where $\Delta E_{1/2}$ is the difference in redox potentials associated with the first and second oxidation of the metal centers. The electrochemical response of binuclear transition metal complexes bridged with polyynes and related ligands derived from polyynes (μ-C≡C–X–C≡C, X = C≡CC≡C, 1,4-C_6H_4, 2,5-thiophene, and 2,5-pyridine) has been comprehensively studied. The compounds [(η^5-C_5Me_5)Re(NO)(PPh_3)]$_2$(μ-C≡C)$_n$ (n = 2, 3 and 4) [21–24] display reversible electrochemical response, the cyclic voltammogram (CV) of these compounds being characterized by two one-electron redox waves. Furthermore, the decreasing of the $\Delta E_{1/2}$ value from 0.53 V in n = 2, 0.38 V in n = 3 to 0.28 V in n = 4 indicates that the magnitude of Re^{2+}–Re^{2+} interaction is decreased significantly on the number of C≡C moiety. Furthermore, complexes with an odd numbered carbon linear or cyclic bridge has been recently found to promote very efficient electronic communication between two [$RuCl(dppe)_2$]$^+$ metal centers [25].

Very recently, we have described the electrochemical and photophysical properties for a series of complexes containing

* Corresponding author. Tel.: +886 7 5253937; fax: +886 7 525 3908.
E-mail address: dty@mail.nsysu.edu.tw (T.-Y. Dong).

0022-328X/$ - see front matter © 2009 Elsevier B.V. All rights reserved.
doi:10.1016/j.jorganchem.2008.12.056

bis-(2,2′:6′,2″-terpyridyl)polyferrocene redox-active spacers end-capped with photoactive and redox-active Ru^{2+}-terpyridine terminals ($[(tpy)Ru^{II}$-(tpy-$(fc)_n$-tpy)-$Ru^{II}(tpy)]^{4+}$ (tpy = terpyridine, fc = ferrocenyl, n = 1–3) and $[(tpy)Ru^{II}$-(tpy-C≡C-$(fc)_n$-C≡C-tpy)-$Ru^{II}(tpy)]^{4+}$ (n = 2–3)) to study the electronic interaction between the end-capped Ru^{2+} metal centers [26–28]. In our previous papers, the CV electrochemical measurements for these binuclear Ru^{2+} complexes were dominated by the Ru^{2+}/Ru^{3+} redox couple ($E_{1/2}$ from 1.35 to 1.38 V), Fe^{2+}/Fe^{3+} redox couples ($E_{1/2}$ from 0.4 to 1.0 V) and $tpy/tpy^{-}/tpy^{2-}$ redox couples ($E_{1/2}$ from −1.3 to −1.5 V). Note worthily, a single irreversible wave was found for the Ru^{2+}/Ru^{3+} redox couple. We suggested that the electronic coupling between the two Ru^{2+} centers is relatively weak. In attempting to modulate the electronic coupling between the two terminal Ru^{2+} centers by manipulation of the energetic of the end-capped metal centers and the connecting spacer, we now describe the electrochemical and photophysical properties of **1**–**7** (Schemes 1 and 2). The preparation and X-ray crystallographic structure analysis of **1** were previously reported by Bruce [19]. Quasi-reversible and irreversible waves were observed in the cyclic voltammetry (CV) measurements of complexes **1**. Our design principle for wire-like molecules **1**–**5** is that the redox-active ferrocenyl–ethynyl spacer can enhance the capability of transfer information along the stepwise molecular axis through stronger σ-bonding of M^{2+}–C≡C in comparison with tpy-ferrocenyl-tpy spacer. Furthermore, it has been found that the 18-electron ferrocene complex can be easily oxidized to form a stable 17-electron ferrocenium complex. As shown in Scheme 3, rapid intramolecular electron transfer between the two ruthenium centers in mixed-valence diruthenium complex could occur through the ferrocenyl spacer. Thus, the ferrocenyl spacer that can provide an effective hetero-nuclear electron delocalization along main chain can serve as model system for molecular wire.

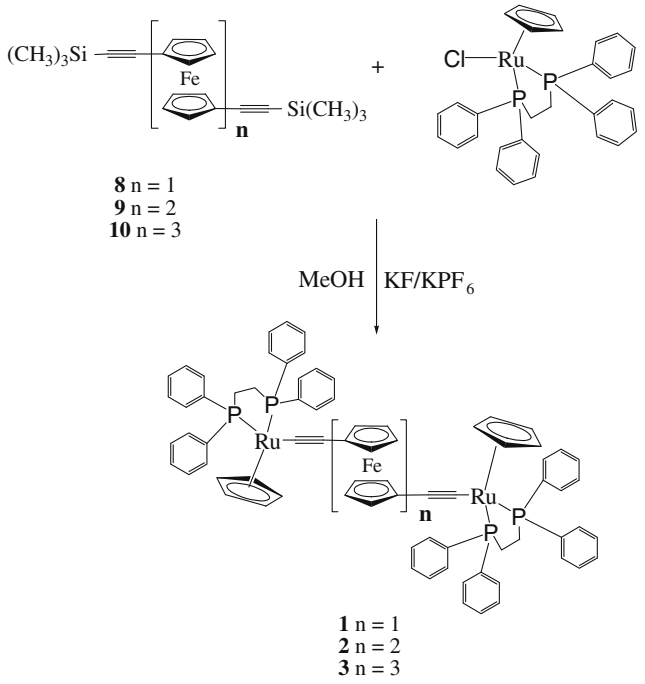

Scheme 1. Synthesis of the discussed Ru^{2+} complexes with ferrocenyl–ethynyl spacers.

2. Results and discussion

2.1. Synthesis and characterization

Binuclear complexes of **1**–**7** were prepared by reacting ferrocenylethynyl spacers (**8**–**12**) with stoichiometric amount of $(\eta^5$-$C_5H_5)$(dppe)MCl. Complexes were purified by column chromatography and recrystallization. All complexes were fully characterized by 1D and 2D NMR techniques, IR, MS and elemental analysis. Structures of complexes **1**–**5** were characterized by ^{31}P NMR showing a singlet for the four equivalent phosphorus nuclei at ~87 ppm in the $[Ru(\eta^5$-$C_5H_5)L_2]$ end-capped complexes (**1**–**3**) and at ~107 ppm in the $[Fe(\eta^5$-$C_5H_5)L_2]$ end-capped complexes (**4**–**5**). The ethynyl carbons in **1**–**3** were identified by ^{13}C NMR showing a singlet at ~107 ppm for the carbon bonded to the ferrocenyl

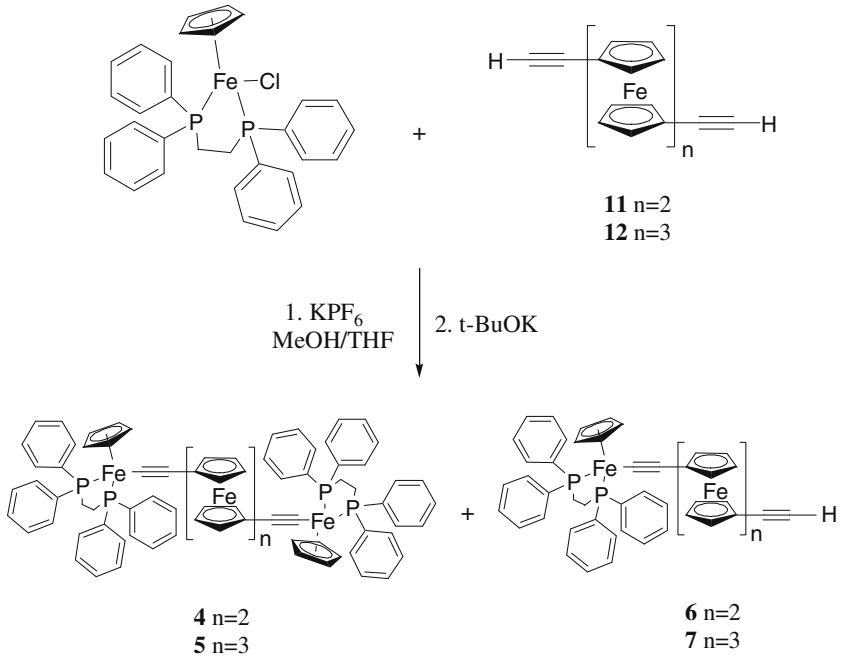

Scheme 2. Synthesis of the discussed Fe^{2+} complexes with ferrocenyl–ethynyl spacers.

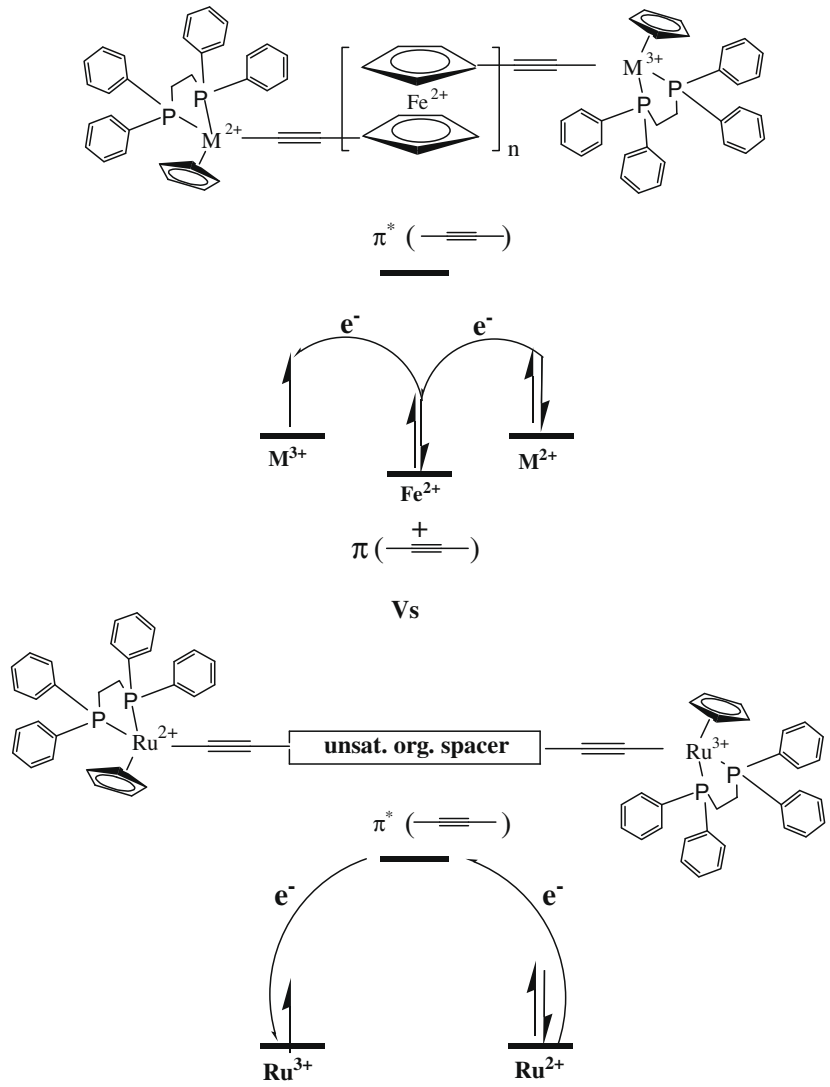

Scheme 3. Intramolecular electron transfer between the two ruthenium centers in a mixed-valence diruthenium complex through ferrocenyl spacer or through unsaturated organic spacer.

moiety and a triplet ~106 ppm for the carbon bonded to the Ru^{2+} metal ($^2J_{PC}$ = ~25 Hz). In the case of [Fe(η^5-C_5H_5)L_2] end-capped complexes, the ethynyl carbons were also identified by ^{13}C NMR showing a singlet at ~116 ppm for the carbon bonded to the ferrocenyl moiety and a triplet ~114 ppm for the carbon bonded to the Fe^{2+} metal ($^2J_{PC}$ = ~42 Hz). The IR spectroscopic data of **1**–**3** also showed the characteristic of triple bond vibration from 2079 to 2089 cm^{-1}. In the case of **4** and **5**, a red-shift of C≡C vibration was observed at 2067 cm^{-1}. Selected spectroscopic data of compounds **1**–**5** are given in Table 1.

2.2. Molecular structure of complex *2*

The X-ray crystallographic structure analysis of **2** showed that its space group was $P2_1/c$ at 120 K. As shown in Fig. 1, the ORTEP view confirms the molecular structure with the ferrocenyl group directly linked to the ethynyl linkage which is linked to the [(η^5-C_5H_5)(dppe)Ru] metal center. Geometry of the [(η^5-C_5H_5)-(dppe)Ru] fragment is similar to those examples reported previously, such as complex of [(η^5-C_5H_5)(dppe)Ru(C≡Cfc)] [29]. Distances of Ru–P (Ru1–P1, 2.2449(5); Ru1–P2, 2.2611(5)) and Ru1–C_{cp} (Ru1–C11, 2.236(2); Ru1–C12, 2.227(2); Ru1–C13, 2.233(2); Ru1–C14, 2.247(2); Ru1–C15, 2.244(2)) are also within previously observed ranges. Based on the angles of P2–Ru1–P1 (83.63(2)°), P1–Ru1–C41 (82.57(5)°), and P2–Ru1–C41 (83.10(5)°), the Ru^{2+} metal center has pseudo-octahedral geometry.

The biferrocenyl moiety exists in a trans conformation with the two iron ions on opposite sides of the fulvalenide ligand. The molecular structure of **2** can be described as step-like of ferrocenyl moieties. The refinement of the structure imposed an inversion center. Thus, the two Ru and Fe centers are crystallographically equivalent and the two Ru-ethynyl axes are parallel. The dihedral angle of Ru–C_6–C_1–$C_{1'}$ (125.4°) indicates that complex **2** does not have linear molecular wire geometry as shown in Fig. 1. The two least-squares-fitting Cp planes in a given ferrocenyl moiety are nearly parallel, and the dihedral angle is 0.86(8)°. Inspection of the average distances of Fe–C (2.048(3) Å) and Fe–Cp (1.6549(2) Å) indicates that the metallocenes are in Fe^{2+} oxidation state [30,31]. The bond distances and angles about the Cp rings vary little and they are close to those reported for analogous ferrocenes. Furthermore, the two Cp rings associated with Fe center are nearly eclipsed, with an average staggering angle of 18.34°. Attachment of ethynyl moiety to the biferrocene has minimal influence

Table 1
Selected spectroscopic data and important bond distances and angles of compounds **1–5.**

Compound	1	2	3	4	5
ν (C≡C stretching, cm^{-1})[a]	2089	2080	2079	2067	2067
M^{2+}–C≡ (^{13}C NMR)[b]	105.18	106.55	107.06	113.75	114.00
fc–**C**≡ (^{13}C NMR)[b]	107.93	107.36	107.44	115.82	115.72
^{31}P NMR[b]	87.10	87.53	87.11	107.13	107.28
C≡C (Å)	1.25(2)[c]	1.203(2)		1.226(9)	
M^{2+}–C≡ (Å)	2.00(1)[c]	2.018(2)		1.883(9)	
M^{2+}–P1	2.259(3)	2.2449(5)		2.153(2)	
M^{2+}–P2	2.254(3)	2.2611(5)		2.133(2)	
M^{2+}–C(Cp) (av. Å)[d]	2.25(2)	2.237(2)		2.083(7)	
Fe–C (av. Å)[e]	2.05(2)[c]	2.048(3)		2.040(7)	
Fe–Cp (centroids, av. Å)[f]	1.64[c]	1.6549(2)		1.648(1)	
Cp–Cp dihedral angle (°)[g]	0.0[c]	0.86		0.67	
Cp–Cp stagger angle (°)[h]		18.34		7.64	
M^{2+}–C≡C (°)	176(1)[c]	178.6(2)		178.4(7)	
P1–M^{2+}–P2 (°)	84.0(1)	83.63(2)		87.16(8)	
P1–M^{2+}–C≡	90.7(4)	82.57(5)		85.3(2)	
P2–M^{2+}–C≡	80.6(3)	83.10(5)		85.4(2)	
M^{2+}/M^{2+} distance (Å)[i]	13.48[c]	19.07	24.64[j]	18.82	24.40[j]

[a] KBr mull.
[b] In C_6D_6.
[c] From Ref. [19]. The structure analysis of **1** was carried out at room temperature.
[d] Average M^{2+}–C(Cp) distance.
[e] Average Fe–C distance for each ferrocenyl moiety.
[f] Distance from the Fe atom to the center of mass of the Cp ring in each ferrocenyl moiety.
[g] Dihedral angle between the two least-squares-fitting Cp ring in each ferrocenyl moiety.
[h] Average stagger angle between the two Cp rings in each ferrocenyl moiety.
[i] The M^{2+}–M^{2+} metal–metal distances (M^{2+}–C6–Fe^{2+}–C1–C1′–Fe^{2+}–C6′–M^{2+}).
[j] For complexes **3** and **5**, the M^{2+}–M^{2+} metal–metal distance was estimated from theoretical geometry generated by optimization.

on the molecular structure in comparison with analogous biferrocene.

The C40–C41 triple bond distance (1.203(2) Å) in ethynyl moiety is slightly longer than that in $[(\eta^5\text{-}C_5H_4)Fe(\eta^5\text{-}C_5H_4C{\equiv}CH)]_2$ (1.176(5) Å) [32], indicating the existence of π characteristic between the Ru^{2+} center and the ethynyl moiety. Furthermore, the triple bond distance in **2** is 0.047 Å shorter than that in **1** [19], indicating an increasing of π characteristic between the Ru^{2+} center and the ethynyl moiety in **1**. The Ru1–C41 (2.018(2) Å) distance involving the ethynyl moiety in **2** is slightly longer than that in **1** (2.00(1) Å). There have been reported that the σ-bonding Ru–C distances are 2.214(5) Å in $[(\eta^5\text{-}C_5H_5)(PPh_3)(PMe_3)Ru\text{–}CH_2(CH(CH_3)_2)]$ and 2.186(9) Å in $[(\eta^5\text{-}C_5H_5)(PMe_3)_2Ru\text{-}CH_2CH_2\text{-}IrCl(\eta^5\text{-}C_5H_5)_2]$ [33,34]. The π characteristic was also evidenced by the red-shift of the triple bond IR stretch from 2149 cm^{-1} in spacer **9** to 2080 cm^{-1} in Ru^{2+} complex **2**. The averaged Ru1–C(Cp) distances in **2**, e.g., Ru1–C(11–15) between 2.227(2) and 2.247(2) Å, is 2.237(2) Å which is similar to that in **1** (2.25(2) Å). As given in Table 1, a direct comparison of **2** with **1** was made. There is little difference between **1** and **2** in ferrocenyl moiety and Ru^{2+}-dppe ligand environment.

2.3. Molecular structure of complex $\mathbf{4}\cdot C_6H_6$

The X-ray crystallographic structure analysis of $\mathbf{4}\cdot\mathbf{C_6H_6}$ showed that its space group was $P2_1/n$ at 150 K. As shown in Fig. 2, the ORTEP view confirms the molecular structure is similar to that of **2** described previously. Distances of Fe2–P (Fe2–P1, 2.153(2); Fe2–P2, 2.133(2)) and Fe2–C_{cp} (Fe2–C11, 2.093(7); Fe2–C12, 2.085(7); Fe2–C13, 2.075(7); Fe2–C14, 2.077(7); Fe2–C15, 2.087(7)) are similar to those of $[(\eta^5\text{-}C_5(CH_3)_5)(dppe)$-

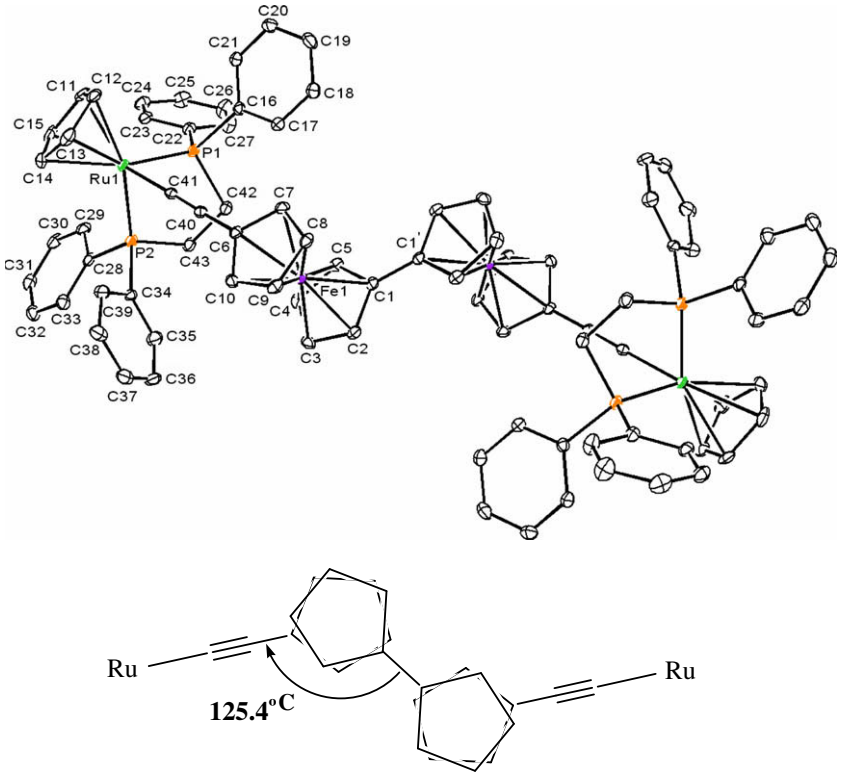

Fig. 1. ORTEP drawing of **2** with the atom-numbering scheme. The determination was carried out at 120.0(1) K. Selected bond distances (Å) and angles (°): Fe–C1, 2.061(2); Fe–C2, 2.050(2); Fe–C3, 2.045(2); Fe–C4, 2.042(2); Fe–C5, 2.039(2); Fe–C6, 2.079(2); Fe–C7, 2.047(2); Fe–C8, 2.032(2); Fe–C9, 2.034(2); Fe–C10, 2.049(2); Ru1–C11, 2.236(2); Ru1–C12, 2.227(2); Ru1–C13, 2.233(2); Ru1–C14, 2.247(2); Ru1–C15, 2.244(2); Ru1–C41, 2.018(2); Ru1–P1, 2.2449(5); Ru1–P2, 2.2611(5); C1–C1′, 1.460(4); C6–C40, 1.442(2); C40–C41, 1.203(2); P2–Ru1–P1, 83.63(2); P1–Ru1–C41, 82.57(5); P2–Ru1–C41, 83.10(5); Ru1–C41–C40, 178.6(2); C41–C40–C6, 177.3(2).

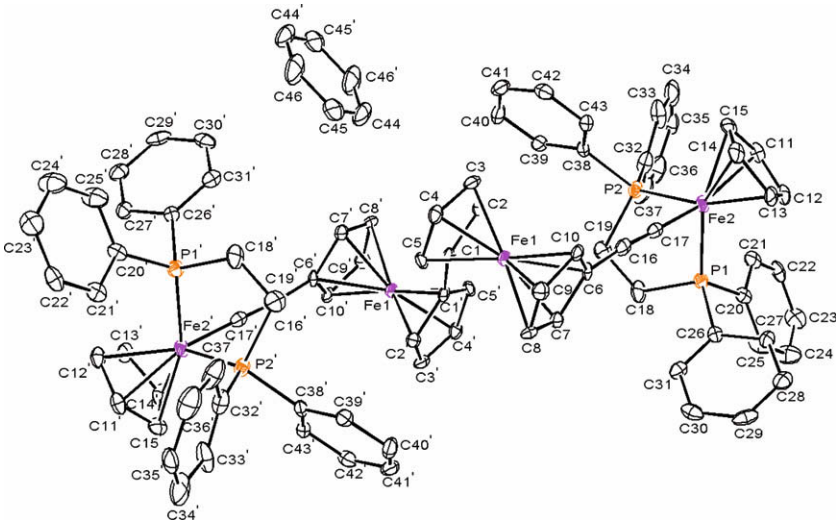

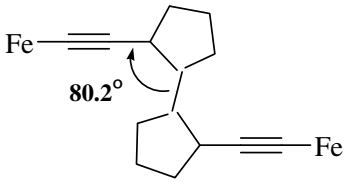

Fig. 2. ORTEP drawing of **4** with the atom-numbering scheme. The determination was carried out at 150.0(1) K. Selected bond distances (Å) and angles (°): Fe1–C1, 2.053(7); Fe1–C2, 2.026(7); Fe1–C3, 2.027(6); Fe1–C4, 2.048(7); Fe1–C5, 2.037(7); Fe1–C6, 2.072(7); Fe1–C7, 2.035(6); Fe1–C8, 2.033(6); Fe1–C9, 2.026(7); Fe1–C10, 2.041(7); Fe2–C11, 2.093(7); Fe2–C12, 2.085(7); Fe2–C13, 2.075(7); Fe2–C14, 2.077(7); Fe2–C15, 2.087(7); Fe2–C17, 1.883(9); Fe2–P1, 2.153(2); Fe2–P2, 2.133(2); C1–C1′, 1.47(1); C6–C16, 1.441(10); C16–C17, 1.226(9); P2–Fe2–P1, 87.16(8); P1–Fe2–C17, 85.3(2); P2–Fe2–C17, 85.4(2); Fe2–C17–C16, 178.4(7); C17–C16–C6, 175.2(7).

Fe(C≡CfcC≡C)Fe(dppe)(η^5-$C_5(CH_3)_5$)] reported previously [19]. Based on the angles of P2–Fe2–P1 (87.16(8)°), P1–Fe2–C17 (85.3(2)°), and P2–Fe2–C17 (85.4(2)°), the end-capped Fe^{2+} metal center has pseudo-octahedral geometry.

The biferrocenyl moiety also exists in a trans conformation. The refinement of the structure imposed an inversion center. Thus, the two end-capped [Fe(η^5-C_5H_5)L_2] centers are crystallographically equivalent and the two Fe-ethynyl axes are parallel. The dihedral angle of Fe–C_6–C_1–C_1' (80.20°) indicates that complex **4** does not have linear molecular wire geometry as shown in Fig. 2. The two least-squares-fitting Cp planes in a given ferrocenyl moiety are nearly parallel, and the dihedral angle is 0.67°. Inspection of the average distances of Fe1–C (2.040(7) Å) and Fe1–Cp (1.648(1) Å) indicates that the metallocenes are also in Fe^{2+} oxidation state. Furthermore, the two Cp rings associated with Fe center are nearly eclipsed, with an average staggering angle of 7.64°.

The C16–C17 triple bond distance (1.226(9) Å) in ethynyl moiety is slightly longer than that in **2** (1.203(2) Å), indicating the existence of more π characteristic between the [Fe(η^5-C_5H_5)L_2] metallic center and the ethynyl moiety. The more π characteristic was also evidenced by the red-shift of the triple bond IR stretch from ~2085 cm^{-1} in **1–3** to 2067 cm^{-1} in **4–5**. As given in Table 1, a direct comparison of **2** with **4** was also made.

2.4. Electrochemical measurements of complexes *1–7*

One of the interesting attributes of **1–5** is the magnitude of the interaction between the two terminal metallic sites. Electrochemical voltammetry affords a simple and effective way for estimating this interaction. In this study, DPV measurements of **1–5** were carried out in anhydrous CH_2Cl_2 solution. The electrochemical results for **1–5** and the spacers are given in Table 2. As shown in Fig. 3, the redox behavior in **1** and **2** is dominated by the two reversible Ru^{2+}/Ru^{3+} redox couples ($E_{1/2}$ at 0.05 and 0.57 V in **1**; 0.10 and 0.27 V in **2**) and reversible ferrocene-based Fe^{2+}/Fe^{3+} redox couples ($E_{1/2}$ at 0.86 V in **1**; 0.73 and 0.87 V in **2**) vs. Ag/AgCl. For complex **3**, one reversible Ru^{2+}/Ru^{3+} redox couple ($E_{1/2}$ at 0.14 V) and three

Table 2
DPV data of **1–10** with scan rate of 20 mV s^{-1}.[a]

Compound	$M^{2+/3+}$			$Fe^{2+/3+}$		
	$E_{1/2}$ (V)	$\Delta E_{1/2}$ (V)	K_c	$E_{1/2}$ (V)	$\Delta E_{1/2}$ (V)	K_c
1	0.05 0.57	0.52	6.51×10^8	0.86		
2	0.10 0.27	0.17	7.61×10^2	0.73 0.87	0.14	2.36×10^2
3	0.14	0.00	~4[b]	0.62 0.83 0.96	0.21 0.13	3.63×10^3 1.60×10^2
4	0.04	0.00	~4[b]	0.60 0.89	0.29	8.23×10^4
5	0.04	0.00	~4[b]	0.47 0.75 1.02	0.28 0.27	5.57×10^4 3.77×10^4
6	−0.03			0.54 0.86	0.32	2.65×10^5
7	−0.04			0.38 0.72 0.98	0.34 0.26	5.79×10^5 2.55×10^4
8				0.81		
9				0.60 0.97	0.37	1.87×10^6
10				0.42 0.78 1.07	0.36 0.29	1.26×10^6 8.23×10^4

[a] $E_{1/2}$: all half-wave potentials are referred to the Ag/AgCl electrode in anhydrous CH_2Cl_2 solution. $\Delta E_{1/2}$: the difference of $E_{1/2}$ between two redox waves of metal centers. K_c: disproportionation constant $K_c = 10^{\Delta E(1/2)/0.059}$.
[b] In the statistical limit.

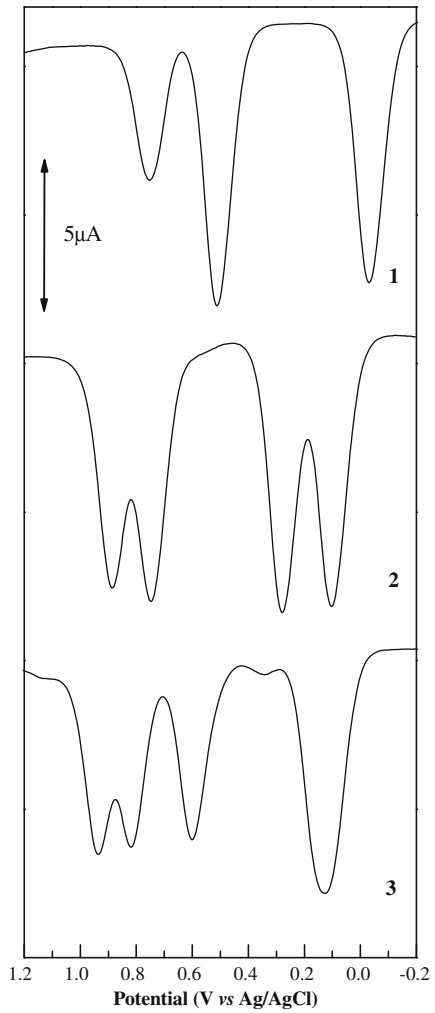

Fig. 3. Electrochemical measurements of **1–3** in CH_2Cl_2 at room temperature vs. Ag^+/AgCl.

reversible ferrocene-based Fe^{2+}/Fe^{3+} redox couples ($E_{1/2}$ at 0.62, 0.83, 0.96 V) vs. Ag/AgCl were observed.

Quasi-reversible and irreversible waves were observed in the CV measurements of complexes **1** [20], [(η^5-C_5H_5)(PPh_3)$_2$Ru–C≡C–Ph] [35], [(η^5-C_5H_5)(PPh_3)$_2$Ru–C≡C–fc] (fc = ferrocenyl) [30], and [(η^5-C_5H_5)(dppe)Ru–C≡C–fc]. Therefore, differential pulse voltammetry was employed to obtain better-resolved potential information in our study, because the Fe^{2+}/Fe^{3+} redox process for **2** and **3** was quasi-reversible in the CV experiment. In our CV voltammograms of **4–7,** reversible Ru^{2+}/Ru^{3+} and Fe^{2+}/Fe^{3+} redox couples were observed in these complexes. In the case of [(η^5-C_5H_5)(dppe)Ru–C≡C–fc], a quasi-reversible wave at $E_{1/2}$ = −0.16 V and a irreversible wave at E_{pa} = 0.48 V vs. Ag/AgCl were observed in Sato's previous report [29]. An additional cathodic wave was observed at E_{pc} = 0.35 V, but this wave was small or vanishing when the scanning turned back. Furthermore, it was unambiguously assigned from the solid-state Mössbauer result that the low-potential wave was assigned to the Fe^{2+}/Fe^{3+} redox couple of the ferrocenyl moiety. The solid-state Mössbauer spectrum of one-electron-oxidized complex [(η^5-C_5H_5)($P(Ph)_3$)$_2$Ru–C≡C–fc]$^+$ showed one doublet with quadrupole splitting value of 0.77 mm s^{-1} and isomer shift value of 0.54 mm s^{-1} at 78 K. The smaller quadrupole splitting value in comparison with neutral [(η^5-C_5H_5)(dppe)Ru–C≡C–fc] suggested that the oxidized site was assigned to the iron metal center in ferrocenyl moiety.

In the CV measurement of complex **1**, two reversible waves at −0.03 and 0.50 V and one irreversible wave at 0.81 V vs. Ag wire pseudo-reference electrode were observed by Bruce and his coworkers and the assignment of the waves to the redox reaction of a particular metal center could not be definitely accomplished.

We suggest that the low-potential wave(s) in **1–5** could be assigned to the end-capped metallic centers. In our study, the 2:1:1 integrated area-ratio of the redox couples at half-potential ($E_{1/2}$) of 0.04, 0.60 and 0.89 V in the DPV of **4** and the 2:1:1:1 integrated area-ratio of the redox couples at $E_{1/2}$ of 0.04, 0.47, 0.75, and 1.02 V in the DPV of **5** suggest that the low-potential wave could be assigned to the end-capped metallic centers. Making a comparison with monocapped complexes of **6** and **7**, this assignment of the Fe^{2+}/Fe^{3+} redox couples for the end-capped [(η^5-C_5H_5)(dppe)Fe] moieties at low-potential wave in **4–5** can be further supported. As shown in Fig. 4, the integrated area-ratio of the redox couples at half-potential ($E_{1/2}$) of −0.03, 0.54 and 0.86 V in the DPV of monocapped complex of **6** was varied from 1:1:1 in **6** to 2:1:1 in **4**. The integrated area-ratio was varied from 2:1:1:1 in **5** to 1:1:1:1 in **7**. Furthermore, making a comparison of the redox potentials with the corresponding the free spacer also suggest that the low-potential wave could be assigned to the end-capped metallic centers. This assignment is not in agreement with the solid-state Mössbauer observation for one-electron-oxidized complex [(η^5-C_5H_5)(dppe)Ru–C≡C–fc]$^+$. The DPV measurements

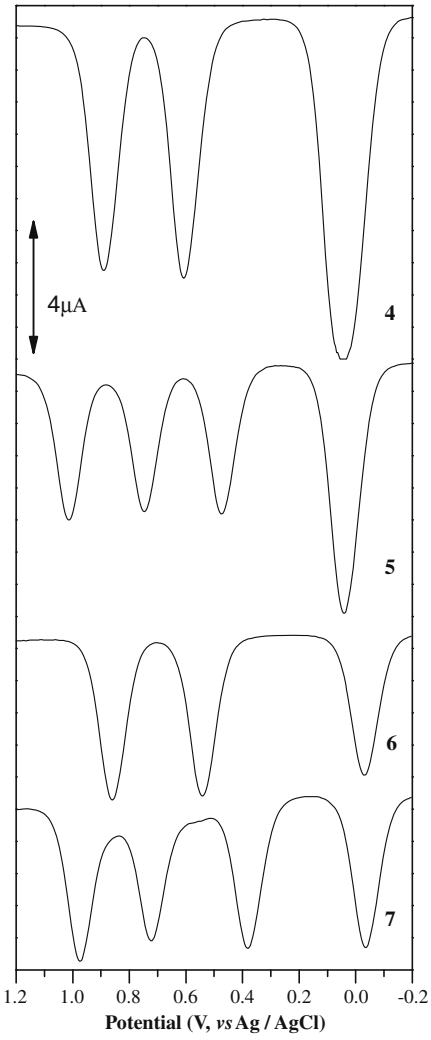

Fig. 4. Electrochemical measurements of **4–5** in CH_2Cl_2 at room temperature vs. Ag^+/AgCl.

of **1**–**5** demonstrate that the σ and π bonding characters of the end-capped metal centers play significantly important role in determining the magnitude of electronic coupling. By replacing the (η^5-C_5H_5)(dppe)Ru center to (η^5-C_5H_5)(dppe)Fe center, a single reversible wave was found for the Fe^{2+}/Fe^{3+} redox couple of end-capped metal centers in **4** and **5**, indicating relatively weak electronic coupling between the two end-capped metallic centers. Finally, the assignment of the Ru^{2+}/Ru^{3+} redox couples in **1**–**3** at high-potential waves can be further excluded, because the metal-to-metal interaction between the two Ru centers should be inversely proportional to the distance between them. Hence, the $\Delta E_{1/2}$ value, giving an indication of the interaction between the two metal sites, should decrease fairly with distance. The assignment of the wave to a particular metal center in complexes **1**–**3** could also be accomplished by comparison with the redox potentials of the analogous complexes. Complex [(η^5-C_5H_5)(PPh_3)$_2$Ru–C≡C–Ph] afforded one redox wave in a similar potential region ($E_{1/2}$ = 0.535 V vs. SCE). Furthermore, complex [(η^5-C_5H_5)(dppe)Ru–C≡C–Ph] afforded one quasi-reversible redox wave in a similar potential region ($E_{1/2}$ = 0.50 V in CH_2Cl_2 vs. SCE). In the case of unsaturated organic spacers, complex (η^5-C_5H_5)(dppe)Ru^{II}–C≡C–C≡C–Ru^{II}(dppe)(η^5-C_5H_5) shows two reversible Ru^{2+}/Ru^{3+} redox couples at $E_{1/2}$ of −0.24 and 0.35 V vs. SCE [36].

Noticeably, pronounced Ru^{2+}–Ru^{2+} metal-to-metal interaction is evidenced directly from the observation of two reversible Ru^{2+}/Ru^{3+} redox couples in **1** and **2**. Making a comparison of the $\Delta E_{1/2}$ values of **1**–**2** with those of [(tpy)Ru^{II}–(tpy-C≡C–(fc)$_n$–C≡C–tpy)–Ru^{II}(tpy)]$^{4+}$ indicates that the interactions between the two Ru^{2+} sites in **1**–**2** are all pronouncedly larger. Furthermore, the decreasing of the $\Delta E_{1/2}$ value from 0.52 V in **1**, 0.17 V in **2** to 0.0 V in **3** indicates that the magnitude of Ru^{2+}–Ru^{2+} interaction is changed significantly on the number of ferrocenyl moieties. The smaller value of $\Delta E_{1/2}$ gives an indication of smaller Ru^{2+}–Ru^{2+} interaction. As shown in Table 1, we have found that there is a correlation between the $\Delta E_{1/2}$ values and the Ru^{2+}–Ru^{2+} metal–metal distances (13.48 Å in **1**, 19.07 Å in **2**, and 24.64 Å in **3**). Metal-to-metal electronic interaction decreases as the Ru^{2+}–Ru^{2+} distance increases. The Ru^{2+}–Ru^{2+} metal–metal distances (Ru^{2+}–C_{cp}–Fe^{2+}–C_{cp}–Ru^{2+}) in **1** and **2** could be directly calculated from the molecular structure determination. For complex **3**, the Ru^{2+}–Ru^{2+} metal–metal distance of 24.64 Å was calculated from the theoretical geometry of **3** generated from the X-ray molecular structure of **2** by setting an inversion center at the Fe center for the fragment of (η^5-C_5H_5)(dppe)Ru^{II}–C≡C–fc–(η^5-C_5H_4)Fe.

As given in Table 2, the comproportionation constants K_c derived from Eq. (1) for the Ru^{2+}/Ru^{3+} redox couples are calculated to be 6.51×10^8 in the mixed-valence **[1]**$^+$, 7.61×10^2 in **[2]**$^+$, and very small value (∼4) for **[3]**$^+$. With increasing Ru–Ru metal distance on going from **[1]**$^+$ to **[3]**$^+$ the thermal stability of the mixed-valence complex decreases sharply to ∼4 for **[3]**$^+$. Better electronic coupling was observed in C_4-alkynyl (η^5-C_5H_5)(dppe)R-u^{II}–(C≡C)$_2$–Ru^{II}(dppe)(η^5-C_5H_5) ($E_{1/2}$ at −0.24 and 0.35 V vs. SCE; $K_c = 1.0 \times 10^{10}$) with Ru^{2+}–Ru^{2+} distance of 7.74 Å [36]. Replacing the (η^5-C_5H_5)(dppe)Ru^{II} metal center by more electron rich (η^5-C_5Me_5)(dppe)Fe^{II} center exhibits higher K_c value (1.6×10^{12}). The electron rich C_5Me_5 ligand enhanced markedly the stability of the mixed-valence state. An adequate comparison of our **[1]**$^+$ system would be with C_8-alkynyl systems [M–(C≡C)$_4$–M] (metal–metal distance ∼13 Å) [37]. System of C_8-alkynyl with (η^5-C_5H_5)(dppe)Ru^{II} metal center has not been reported. Both C_4- and C_8-alkynyl systems have been studied for M = [(η^5-C_5Me_5)Re(NO)(PPh_3)]. The study has revealed that K_c value decreases dramatically from C_4 ($\Delta E_{1/2}$: 0.53 V; K_c: 9.62×10^8) to C_8 ($\Delta E_{1/2}$: 0.28 V; K_c: 5.57×10^4). In the case of electron rich (η^5-C_5Me_5)-(dppe)Fe^{II} metal center, K_c value also decreases dramatically from C_4 (1.6×10^{12}) to C_8 (2.0×10^7). Another adequate comparison of our **[2]**$^+$ system (Ru^{2+}–Ru^{2+} distance = 19.07 Å) would be with C_{14}-alkynyl systems [M–(C≡C)$_7$–M]. The synthesis and molecular structure of C_{14}-alkynyl with electron rich (η^5-C_5Me_5)(dppe)Ru^{II} metal center have been reported. However, the electrochemical measurement has not been reported in this C_{14}-alkynyl complex with Ru^{2+}–Ru^{2+} distance of 20.560(5) Å [38]. Thus, ferrocenyl–ethynyl spacers appear to be promising spacers which can ensure stronger coupling between two Ru^{2+} metal centers. Furthermore, there is a correlation of the $\Delta E_{1/2}$ values with the C≡C stretching values or with the ^{13}C NMR chemical shifts of Ru^{2+}–**C**≡ in **1**–**5**. From Table 1, the $\Delta E_{1/2}$ value decreases as the C≡C stretching value decreases and the ^{13}C NMR chemical shift of Ru^{2+}–**C**≡ increases.

$$[\mathrm{Ru{-}C{\equiv}C{-}(fc)_n{-}C{\equiv}C{-}Ru}] + [\mathrm{Ru{-}C{\equiv}C{-}(fc)_n{-}C{\equiv}C{-}Ru}]^{2+} \overset{K_c}{\rightleftharpoons} 2[\mathrm{Ru{-}C{\equiv}C{-}(fc)_n{-}C{\equiv}C{-}Ru}]^{+} \quad (1)$$

$$K_c = 10^{\Delta E(1/2)/0.059}.$$

Another interesting attributes of **1–5** is the magnitude of the electronic interaction between the Fe sites. As shown in Figs. 3 and 4, complexes **1–5** show reversible oxidation processes on sweeping at anodic potentials between ∼0.6 V and ∼1.0 V, corresponding to the oxidation of the ferrocenyl moieties. When the redox behavior occurred at the ferrocenyl site, the ruthenium metal center should be in the Ru^{3+} oxidation state. We found that there was appreciable variation detected in the potential associated with each Fe^{2+}/Fe^{3+} redox couple. Furthermore, the variation of the $\Delta E_{1/2}$ value for the $Fe^{2+/3+}$ redox couples (0.37 V in the free spacer **9,** 0.14 V in its Ru^{2+} complex **2** and 0.29 V in its Fe^{2+} complex **4**; 0.36 and 0.29 V in the free spacer **10**, 0.21 and 0.13 V in its Ru^{2+} complex **3** and 0.28 and 0.27 V in its Fe^{2+} complex **5**) strongly suggest that there is an interaction between the iron and the ruthenium metal centers. The decreasing of Thus, ferrocenyl–ethynyl spacers appear to be promising spacers which can ensure stronger coupling between two Ru^{2+} metal centers. Furthermore, there is a correlation of the $\Delta E_{1/2}$ values with the C≡C stretching values or with the ^{13}C NMR chemical shifts of Ru^{2+}–**C**≡ in **1–5**. From Table 1, the $\Delta E_{1/2}$ value decreases as the C≡C stretching value decreases and the ^{13}C NMR chemical shift of Ru^{2+}–**C**≡ increases value for the $Fe^{2+/3+}$ redox couples in **1–5** indicates that the magnitude of Fe–Fe interaction is changed pronouncedly on the coordination of Ru^{3+} ion. The smaller value of $\Delta E_{1/2}$ gives an indication of smaller Fe–Fe interaction. Due to the electronic coupling between the iron and the ruthenium metal centers, the hetero-nuclear electron transfer process between the Fe^{2+} and Ru^{3+} nuclei is possible. As an example, on the oxidation to the monocation **[2]**$^+$, more than one oxidation isomer can exist. In monocation **[2]**$^+$, an equilibrium can exist between the two energetically nonequivalent isomers Ru_a^{3+}–Fe_a^{2+}–Fe_b^{2+}–Ru_b^{2+} ↔ Ru_a^{2+}–Fe_a^{2+}–Fe_b^{2+}–Ru_b^{3+} and Ru_a^{2+}–Fe_a^{3+}–Fe_b^{2+}–Ru_b^{2+} ↔ Ru_a^{2+}–Fe_a^{2+}–Fe_b^{3+}–Ru_b^{2+}. The distribution between the two isomers depends on the zero-point energy difference between them. Energetically, the energy surface for the two equivalent isomers Ru_a^{3+}–Fe_a^{2+}–Fe_b^{2+}–Ru_b^{2+} and Ru_a^{2+}–Fe_a^{2+}–Fe_b^{2+}–Ru_b^{3+} is more stable than that for the 2 equiv. isomers Ru_a^{2+}–Fe_a^{3+}–Fe_b^{2+}–Ru_b^{2+} and Ru_a^{2+}–Fe_a^{2+}–Fe_b^{3+}–Ru_b^{2+}. In dication **[2]**$^{2+}$, oxidation isomers Ru_a^{3+}–Fe_a^{2+}–Fe_b^{2+}–Ru_b^{3+}, Ru_a^{3+}–Fe_a^{2+}–Fe_b^{3+}–Ru_b^{2+}, Ru_a^{3+}–Fe_a^{3+}–Fe_b^{2+}–Ru_b^{2+}, Ru_a^{2+}–Fe_a^{3+}–Fe_b^{2+}–Ru_b^{3+}, Ru_a^{2+}–Fe_a^{2+}–Fe_b^{3+}–Ru_b^{3+}, and Ru_a^{2+}–Fe_a^{3+}–Fe_b^{3+}–Ru_b^{2+} could be in a state of equilibrium.

2.5. IR, EPR, and UV spectra of oxidation complexes [1]$^+$ and [2]$^{2+}$

Thermodynamic stability of the oxidized forms with respect to the disproportionation constants was matched and chemical

oxidation with ferrocenium PF_6 allowed isolation of monooxidized complex of **[1]**$^+$ and dioxidized complex of **[2]**$^{2+}$ as PF_6^- salts in essentially quantitative yield. Due to the smaller $\Delta E_{1/2}$ and K_c values, pure monooxidized complex of **[2]**$^+$ could not be synthesized successfully by chemical oxidation. To understand which metal site was oxidized, the *solid-state* and *solution-state* electronic configurations in multinuclear complexes of **[1]**$^+$ and **[2]**$^{2+}$ were characterized by IR, X-band EPR spectroscopy, and UV–Vis at room temperature and 77 K.

IR spectroscopy has proven to be useful to tell which metal site is oxidized. When Fe^{2+} metallocene is oxidized to Fe^{3+} metallocene, there is a dramatic change in the IR spectrum. The perpendicular C–H bending band of the ferrocenyl moiety is the best diagnosis of the oxidation state. In solid-state, this band is seen at 815 cm^{-1} for ferrocene and at 851 cm^{-1} for ferrocenium triiodide [39]. Infrared spectra were run for KBr pellets for **[1]**$^+$ and **[2]**$^{2+}$. For the perpendicular C–H bending region there are relatively strong bands appeared at 838 and 840 cm^{-1} for **[1]**$^+$ and **[2]**$^{2+}$, respectively. This observation suggests that the Fe metallic center in solid-state complexes of **[1]**$^+$ and **[2]**$^{2+}$ is in Fe^{3+} oxidation state. Upon oxidation of **1** to **[1]**$^+$, the stretching vibration of C≡C at 2089 cm^{-1} in **1** disappears and a strong band appears at 1998 cm^{-1} in **[1]**$^+$. This band is intermediate between the stretching vibration of C≡C (~2070 cm^{-1}) and that of =C=C= (~1926 cm^{-1}). Furthermore, the IR spectra of **[2]**$^{2+}$ showed a strong absorption of C≡C at 1988 cm^{-1}. The oxidized complexes of **[1]**$^+$ and **[2]**$^{2+}$ are considerably stable in solid-state. In Bruce's study [19], spectroelectrochemically generated IR spectrum of oxidized complex of **[1]**$^+$ resulted in a lower energy shift of the stretching vibration of C≡C at 1986 and 2030(sh) cm^{-1}. The IR data suggests a substantial electron delocalization over the (η^5-C_5H_5)(dppe)Ru metal center and ferrocenyl center.

As shown in Fig. 5, the appearance of the absorption bands at 600 and 607 nm in the UV spectra of **[1]**$^+$ (ε = 6340 M^{-1} cm^{-1}) and **[2]**$^{2+}$ (ε = 3933 M^{-1} cm^{-1}) in CH_2Cl_2 solution at 298 K would further support that there is a substantial electron delocalization over the metal centers. This absorption band, which is not present in the neutral complexes of **1** and **2**, was assigned to the ligand-to-metal (Cp-to-Fe^{3+}) $^2E_{2g} \rightarrow {}^2E_{1u}$ transition. In the mono-ruthenium complex of [(η^5-C_5H_5)(PPh_3)$_2$Ru–(C≡C)–fc]$^+$ with Fe^{3+} character identified by solid-state Mössbauer technique, an absorption band at 605 nm (ε = 8800 M^{-1} cm^{-1}) was observed in CH_2Cl_2 solution at room temperature. In our case, the appearance of this lower intensity absorption in comparison with the mono-ruthenium complex of [(η^5-C_5H_5)(PPh_3)$_2$Ru–(C≡C)–fc]$^+$ indicates that the iron metal center has some degree of Fe^{3+} character.

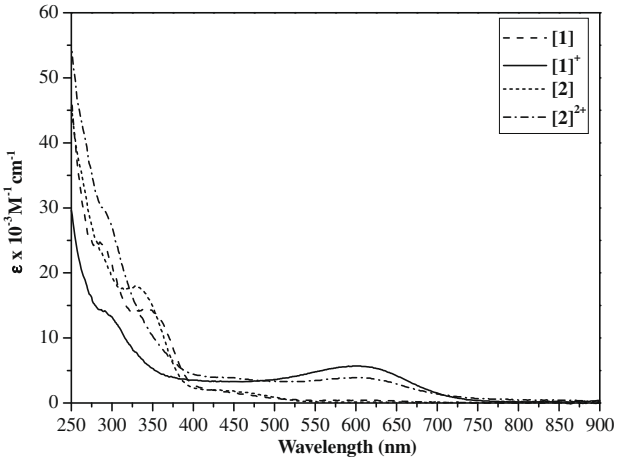

Fig. 5. UV spectra of **1**, **2**, **[1]**$^+$ and **[2]**$^{2+}$ in CH_2Cl_2 at room temperature.

As shown in Fig. 6, an axial-type EPR spectrum ($g_\parallel$ = 2.92; $g_\perp$ = 1.95) at 77 K was found for **[1]**$^+$ which did not show any hyperfine splitting. EPR data of (η^5-C_5H_5)(dppe)Ru^{II}–(C≡C)$_n$–Ru^{II}(dppe)(η^5-C_5H_5) or comparable ruthenium complexes with same geometry have not been reported so far. For a mononuclear ferrocenium triiodide with E_{2g} electronic configuration, an axial-type spectrum was observed with $g_\parallel$ = 4.35; $g_\perp$ = 1.26 at 20 K but cannot be seen at room temperature [40]. In the case of a binuclear mixed-valence biferrocenium cation, the value of g tensor anisotropy ($\Delta g = g_\parallel - g_\perp$) is considerably reduced and this is a reflection of admixture of the S = 0 Fe^{2+} A_{1g} electronic configuration into the ground state. It is, therefore, probably reasonable that the oxidized site in **[1]**$^+$ in solid-state at 77 K could be assigned to the ferrocenium Fe^{3+} metal center. Here, we would suggest that reduced Δg value results from the extensive mixing with the Ru^{2+} metal orbital into the Fe^{3+} ground state, as found in electrochemical measurement and molecular calculation. Under this circumstance the iron metal center loses some degree of their Fe^{3+} character. In other words, the admixture of the S = 0 Fe^{2+} electronic configuration has to be included. In the case of solid-state **[2]**$^{2+}$, an axial-type EPR spectrum ($g_\parallel$ = 2.89; $g_\perp$ = 2.04) was also found at 77 K, indicating electron localization at the Fe^{3+} metal center on the EPR timescale (<~10^{10} s^{-1}). As temperature was increased to 298 K, solid-state complexes of **[1]**$^+$ and **[2]**$^{2+}$ are EPR silent, indicating a faster electron relaxation process for the E_{2g} electronic configuration in ferrocenium center and perhaps a rapid electron delocalization over the Ru metal centers and the Fe metal center(s) in ferrocenyl–ethynyl spacers.

Complexes of **[1]**$^+$ and **[2]**$^{2+}$ in CH_2Cl_2 solution at 77 K and 298 K are EPR silent. At 298 K in solution-state, we suggest that the unpaired electron is mainly localized on the Ru^{3+} metal centers.

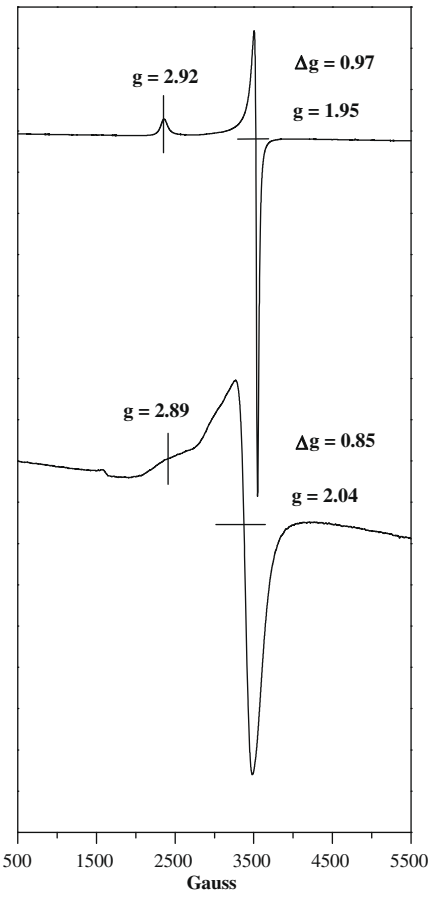

Fig. 6. Solid-state EPR spectra of **[1]**$^+$ (top) and **[2]**$^{2+}$ (bottom) at 77 K.

Due to the rapid electron delocalization over the metal centers, the electron relaxation process is faster than the timescale of EPR technique. Such EPR silence at 298 K in fluid is frequent for Ru^{3+} complexes, such as monocation mixed-valence [Cl(dppe)Ru–C≡C–(C_6H_4–C≡C)$_n$–Ru(dppe)Cl]$^+$ (n = 1, 2, 3). In this arylethynyl system with n = 1, a rhombic EPR spectrum (g = 2.15, 2.05, and 1.99) was only observed in the frozen CH_2Cl_2 solution at 3.4 K [41]. Related 298 K EPR spectrum of mixed-valence C_4-alkynyl iron complex of [(η^5-C_5Me_5)(dppe)Fe–(C≡C)$_2$–Fe(dppe)(η^5-C_5Me_5)]$^+$ has been reported with g_{avg} = 2.126.

2.6. Intervalence transition

As shown in Fig. 7, complexes **[1]**$^+$ and **[2]**$^{2+}$ showed broad intervalence transition (IT) band in the NIR region in CH_2Cl_2 solution. Application of Hush's theoretical analysis [42] of IT band to determine the nature and magnitude of the electronic coupling between the metal sites in complexes **[1]**$^+$ and **[2]**$^{2+}$ is of some interest. Broad intervalence transition (IT) band near 1600 nm (6250 cm^{-1}) could be assigned to the intervalence transition involving photo-induced electron transfer between the two vibronic states of Ru_a^{3+}–Fe^{2+}–Ru_b^{2+} and Ru_a^{2+}–Fe^{3+}–Ru_b^{2+}. In other words, this is an assignment to the intervalence transition between the Ru^{3+} and Fe^{2+} metal centers, indicating the existence of strong metal-to-metal interaction. In the mono-ruthenium complex [(η^5-C_5H_5)(PPh_3)$_2$Ru–(C≡C)–fc]$^+$, a broad absorption band at 1550 nm (ε = 4080 M^{-1} cm^{-1}) was observed in CH_2Cl_2 solution at room temperature. Sato and coworkers suggested that this absorption band, which is not present in the neutral complex [(η^5-C_5H_5)(PPh_3)$_2$Ru–(C≡C)–fc], could be assigned to the intervalence transition between the Ru^{2+} and Fe^{3+} metal centers. They suggested that the iron center was in Fe^{3+} oxidation state based on the solid-state Mössbauer technique.

In our case, the simple two vibronic states model proposed by Hush can not explain the origin of the IT band. As shown in Fig. 8, three and five vibronic states potential energy diagrams are proposed to explain the electronic structures of complexes **[1]**$^+$ and **[2]**$^{2+}$. In **[1]**$^+$, the three potential energy surfaces are related to Ru_a^{3+}–Fe^{2+}–Ru_b^{2+}, Ru_a^{2+}–Fe^{3+}–Ru_b^{2+} and Ru_a^{2+}–Fe^{2+}–Ru_b^{3+}. Applying the Franck-Condon principle, the vertical process indicated by E_{IT} corresponds to the intervalence transition from the ground state Ru_a^{3+}–Fe^{2+}–Ru_b^{2+} to the excited state Ru_a^{2+}–Fe^{3+}–Ru_b^{2+}. Therefore, photoexcitation provides a mechanism for charge transfer across the ferrocenium bis-ethynyl spacer. The upper-limit value of zero-point energy difference (ΔE_0) between

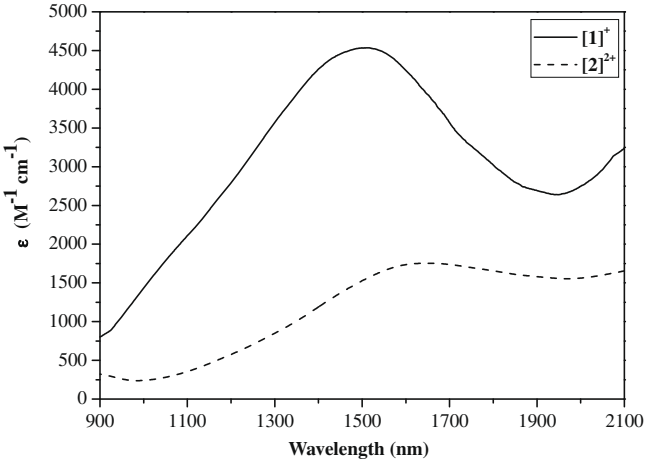

Fig. 7. Intervalence transition band in the NIR region of complexes **[1]**$^+$ and **[2]**$^{2+}$ in CH_2Cl_2 solution.

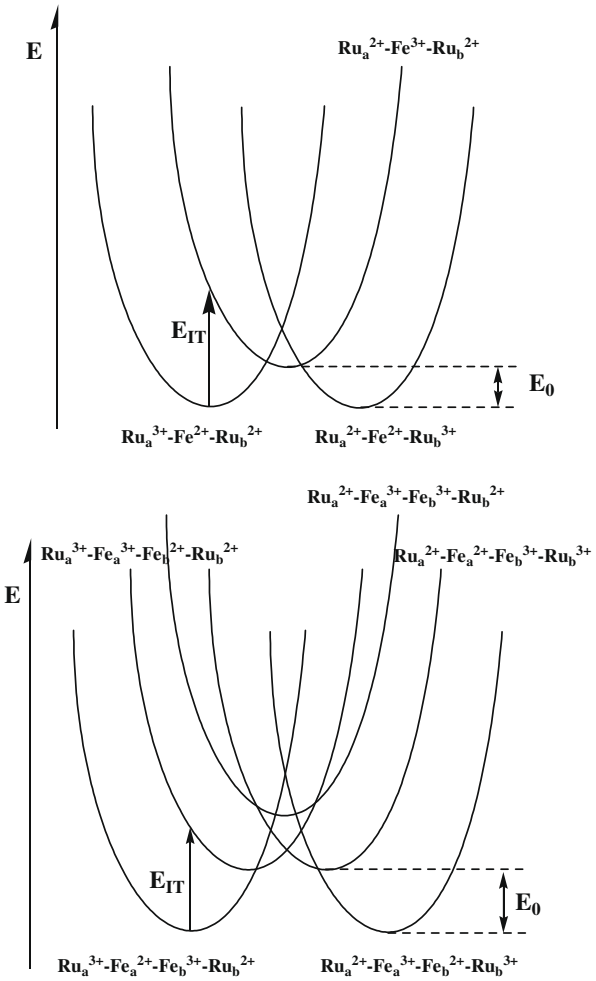

Fig. 8. Potential energy surfaces of **[1]**$^+$ and **[2]**$^{2+}$.

the two vibronic states could be estimated by the difference in the redox potentials of the two metal centers in the molecule. Furthermore, the magnitude of the delocalization can be obtained by a calculation of the delocalization parameter α^2 and electronic coupling V_{ab}. In the case of complexes **[1]**$^+$ and **[2]**$^{2+}$, the values of α^2 and V_{ab} were calculated from the following equations and collected in Table 3. In these equations, ν_{max} is the energy of intervalence transition in cm^{-1}, ε_{max} is the extinction coefficient, $\Delta\nu_{1/2}$ is the band width at half-height observed in cm^{-1}, the constant (4.24×10^{-4}) is in the unit of M cm^{-1}, and d is the donor–acceptor distance in Å. These cations are examples of class II mixed-valence compounds [43].

$$\alpha^2 = \{4.24 \times 10^{-4}\epsilon_{max}(\Delta\nu_{1/2})\}/\{\nu_{max}d^2\},$$

Table 3
Intervalence transition band energies and related data.

Compound	ν_{max}[a]	ε[b]	$\Delta\nu_{1/2}$[c]	α^2 ($\times 10^3$)[d]	V_{ab}[e]
[1]$^+$	6666	4454	4120	25.6	1068
[2]$^{2+}$	6250	1753	2804	7.49	527

[a] ν_{max}: the energy of intervalence transition in cm^{-1}.
[b] Extinction coefficient in M^{-1} cm^{-1}.
[c] $\Delta\nu_{1/2}$: the band width at half-height observed in cm^{-1}.
[d] α^2: delocalization parameter.
[e] V_{ab}: electronic coupling in cm^{-1}.

$V_{ab} = \nu_{max}\alpha$.

2.7. Theoretical calculations

To study the electronic structures of synthesized complexes (**1**–**5**), we have carried out molecular orbital calculations at the B3LYP level of density functional theory to see how the HOMO–LUMO gap correlated with the $\Delta E_{1/2}$. In particular, it is desirable to understand the origin of the Ru^{2+}–Ru^{2+} and Ru^{2+}–Fe^{2+} metal-to-metal interactions from the computational chemistry. For complex **3**, the Ru^{2+}–Ru^{2+} metal–metal distance of 24.64 Å was calculated from the theoretical geometry of **3** generated from the X-ray molecular structure of **2**.

As shown in Fig. 9, examining the characteristics of the five HOMOs (HOMO, HOMO-1, HOMO-2, HOMO-3, and HOMO-4), we found that they commonly correspond to the π orbitals of the ferrocenyl–ethynyl spacers mixed extensively with the d_{x2-y2} orbital of the Ru^{2+} metal center and d_{x2-y2} and d_{xy} orbitals of the Fe^{2+} metal center. In the case of **2**, it is clear that the metallic contribution to the HOMO is mainly from Fe^{2+} centers corresponding to the d_{x2-y2} (10.6%) and d_{xy} (26.4%) orbitals mixed extensively with the P_z orbital (10.6%) of Cp–C≡ and P_z orbital (10.2%) of Ru–C≡, defining the Cp–Fe–Cp axis as the *z*-axis of the Cartesian. The molecular orbital HOMO-1 in **2** is related to the d_{xy} orbital (31.8%) of the Fe^{2+} centers and the P_z orbital (14.6%) of Cp–C≡ and P_z orbital (12.6%) of Ru-C≡. Orbital HOMO-2 is related to the d_{x2-y2} orbital (14.4%) of the Fe^{2+} centers and the d_{x2-y2} orbital (23.8%) of the Ru^{2+} centers.

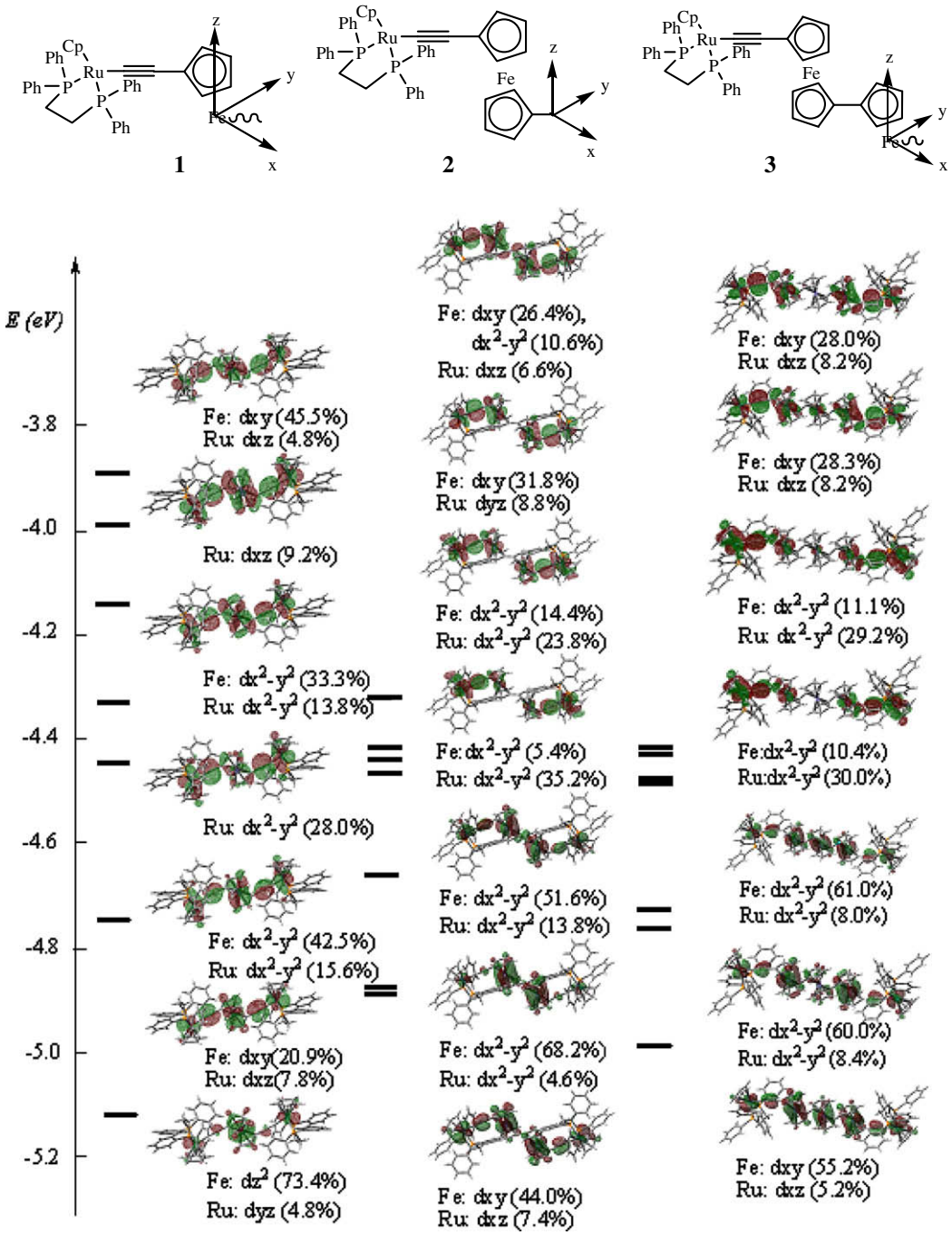

Fig. 9. Representative frontier HOMOs of **1**, **2**, and **3**.

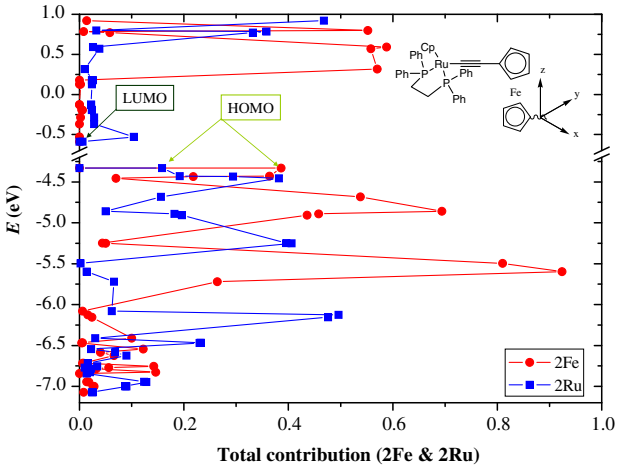

Fig. 10. Total contributions of Ru^{2+} and Fe^{2+} metal centers at any given energy for **2**.

Orbital HOMO-3 is related to the d_{x2-y2} orbital (35.2%) of the Ru^{2+} centers and the P_x (11.4%) and P_y (10.8%) orbitals of Cp–C≡. The molecular orbital HOMO-4 is related to the d_{x2-y2} orbital (51.6%) of the Fe^{2+} centers and the d_{x2-y2} orbital (13.8%) of the Ru^{2+} centers. Molecular calculations indicate a substantial delocalization of the frontier orbital over the metal centers and the ferrocenyl–ethynyl spacers. Fig. 10 shows a typical example of total contribution of Ru^{2+} and Fe^{2+} metal centers at any given energy of **2.** As shown in Fig. 9, examining the characteristics of the four HOMOs in **3**, it is interesting to find that the metallic contribution of the middle ferrocenyl moiety to the HOMO is not found. In other words, the electron delocalization is not continued through the middle ferrocenyl moiety in these HOMOs. We would suggest that this is a possible reflection of the relatively weak electronic coupling between the two Ru^{2+} centers in **3**.

3. Conclusions

Several multinuclear ferrocenyl–ethynyl complexes of formula $[(\eta^5\text{-}C_5H_5)(dppe)M^{II}\text{–}C{\equiv}C\text{–}(fc)_n\text{–}C{\equiv}C\text{–}M^{II}(dppe)(\eta^5\text{-}C_5H_5)]$ were studied. These complexes undergo sequential reversible oxidation events from 0.0 V to 1.0 V referred to the Ag/AgCl electrode in anhydrous CH_2Cl_2 solution. We suggest that the low-potential wave(s) in **1**–**5** could be assigned to the end-capped metallic centers. The resulting oxidation products are characterized by IR, EPR and UV–Vis–NIR spectroscopic methods, suggesting a substantial electron delocalization over the $(\eta^5\text{-}C_5H_5)$(dppe)Ru metal center and ferrocenyl center. A combination of spectroscopic data and computational studies reveals that the ferrocenyl–ethynyl-based orbitals do mix significantly with the $(\eta^5\text{-}C_5H_5)$(dppe)Ru metallic orbitals. It clearly appears from this work that the ferrocenyl–ethynyl spacers quite strongly contribute in propagating electron delocalization.

4. Experimental

4.1. General information

All manipulations involving air-sensitive materials were carried out by using standard Schlenk techniques under an atmosphere of N_2. Solvents were dried as follows: THF and ether were distilled from Na/benzophenone; DMF and CH_2Cl_2 were distilled from CaH_2; TMEDA was distilled from KOH. Samples of **1** and $(\eta^5\text{-}C_5H_5)$(dppe)MCl were prepared according to the literature procedure [44–46]. Preparations of the ferrocenyl–ethynyl spacers (**8**–**10**) were described in our previous paper [26–28]. As shown in Schemes 1 and 2, complexes of **1**–**7** could be prepared.

4.2. Preparation of compound *2*

A mixture of **9** (50 mg, 0.089 mmol), $(\eta^5\text{-}C_5H_5)$(dppe)RuCl (106 mg, 0.178 mmol) [44], and KF (10 mg, 0.178 mmol) was heated in refluxing methanol (40 ml) for 16 h [45]. After cooling to room temperature, the reaction mixture was filtered and washed with methanol, ether, and recrystallized from dichloromethane–hexane to give orange-red solid compound. The yield was approximately 30%. ^{1}H NMR (C_6D_6): δ 2.13–2.24 (m, 4H, -PCHCHP-), 2.72–2.83 (m, 4H, -PCHCHP-), 3.84 (s, 8H, fc-Cp), 3.92 (s, 4H, fc-Cp), 4.16 (s, 4H, fc-Cp), 4.75 (s, 10H, Cp), 6.98 (t, J = 2.0 Hz, 12H, Ph), 7.22–7.25 (m, 12H, Ph), 7.33 (t, J = 7.5 Hz, 8H, Ph), 8.09 (t, J = 8.5 Hz, 8H, Ph). ^{13}C NMR (C_6D_6): δ 29.15 (t, J_{cp} = 23.2 Hz, -PCH_2CH_2P-), 68.53 (s, fc-Cp), 69.34 (s, fc-Cp), 69.82 (s, fc-Cp), 71.59 (s, fc-Cp), 76.84 (s, fc-Cp), 83.21 (s, Cp), 85.32 (s, fc-Cp), 106.55 (t, Ru–C≡, J_{cp} = 25.5 Hz), 107.36 (s, fc–C≡), ~128.00 (s, *m*-Ph, overlap with solvent peak), 129.10, 129.95 (s, *p*-Ph), 132.17 (t, J = 5.0 Hz, *o*-Ph), 135.22 (t, J = 5.0 Hz, *o*-Ph), 137.85–138.32, 143.77–144.22 (m, *ipso*-Ph). ^{31}P NMR (C_6D_6): δ 87.53 (s). MS (ESI): M^+ at m/z 1546.1. Anal. Calc. for $C_{86}H_{74}Fe_2P_4Ru_2$: C, 66.85; H, 4.83. Found: C, 66.82; H, 4.98%. M.p.: 235–237 °C.

4.3. Preparation of compound *3*

A mixture of **10** (50 mg, 0.067 mmol), $(\eta^5\text{-}C_5H_5)$(dppe)RuCl (80.4 mg, 0.134 mmol), and KF (10 mg, 0.178 mmol) was heated in refluxing methanol/THF (3:1) for 16 h. After cooling to room temperature, the solvents were removed in vacuo. The crude product was purified by column chromatography on Al_2O_3 (act. III), eluting with hexane/acetone (9:1). The fourth band was the desired compound. The yield was approximately 10%. ^{1}H NMR (C_6D_6): δ 2.17–2.20 (m, 4H, -PCHCHP-), 2.74–2.77 (m, 4H, -PCHCHP-), 3.73 (s, 8H, fc-Cp), 3.94 (t, 4H, fc-Cp, J = 1.8 Hz), 4.08 (t, 4H, fc-Cp, J = 2.1 Hz), 4.11 (t, 4H, fc-Cp, J = 1.5 Hz), 4.24 (t, 4H, fc-Cp, J = 1.5 Hz), 4.74 (s, 10H, Cp), 6.98 (t, J = 3.0 Hz, 12H, Ph), 7.20–7.25 (m, 12H, Ph), 7.31 (t, J = 7.8 Hz, 8H, Ph), 8.07 (t, J = 8.7 Hz, 8H, Ph). ^{13}C NMR (C_6D_6): δ 29.36 (t, -PCH_2CH_2P-, $J_{c\text{-}p}$ = 23.1 Hz), 68.70 (s, fc-Cp), 68.82 (s, fc-Cp), 69.87 (s, fc-Cp), 70.21 (s, fc-Cp), 71.95 (s, fc-Cp), 77.25 (s, fc-Cp), 83.42 (s, Cp), 84.23 (s, fc-Cp), 86.17 (s, fc-Cp), 107.06 (t, Ru–C≡, J_{cp} = 25.8 Hz), 107.44 (s, fc–C≡), ~128.00 (s, *m*-Ph, overlap with solvent peak), 129.36, 130.19 (s, *p*-Ph), 132.42, 135.42 (s, *o*-Ph), 138.11–138.44, 143.99–144.36 (m, *ipso*-Ph), ^{31}P NMR (C_6D_6): δ 87.11 (s). MS (MALDI-TOF): M^+ at m/z 1730.00. Anal. Calc. for $C_{96}H_{82}Fe_3P_4Ru_2$: C, 66.68; H, 4.78. Found: C, 66.64; H, 4.98%. M.p.: 132–134 °C.

4.4. Preparation of compound *4*

A mixture of **11** (50 mg, 0.12 mmol) [27], $(\eta^5\text{-}C_5H_5)$(dppe)FeCl (200 mg, 0.36 mmol) [46], KPF_6 (130 mg, 0.72 mmol) was stirred in methanol (30 ml) at room temperature. After stirring for 2 h, potassium *tert*-butoxide (56 mg, 0.5 mmol) was added to the solution. The resulting mixture was stirred for a further 15 min. The solvent was removed under reduced pressure. The crude product was purified by column chromatography on Al_2O_3 (act. III), eluting with hexane/acetone (10:1). The first band was mononuclear Fe^{2+} metallic complex (**6**). The yield of **6** was 13%. The second band was the desired complex (**4**). The yield was 58%. Complex of **4** could be recrystallized from benzene–ether to give an orange-red solid compound. The physical properties of **4** are as follows. ^{1}H

NMR (C_6D_6): δ 2.09–2.11 (m, 4H, -PCHCHP-), 2.73–2.76 (m, 4H, -PCHCHP-), 3.85 (s, 4H, fc-Cp), 3.88 (s, 4H, fc-Cp), 3.99 (s, 4H, fc-Cp), 4.22 (s, 4H, fc-Cp), 4.28 (s, 10H, Cp), 6.98–7.02 (m, 12H, Ph), 7.21–7.25 (m 12H, Ph), 7.32 (t, J = 7.5 Hz, 8H, Ph), 8.09 (br s, 8H, Ph). ^{13}C NMR (C_6D_6): δ 29.09 (t, -PCH_2CH_2P-, J = 22.2 Hz), 68.14 (s, fc-Cp), 68.72 (s, fc-Cp), 69.29 (s, fc-Cp), 71.03 (s, fc-Cp), 76.62 (s, fc-Cp), 79.46 (s, Cp), 84.84 (s, fc-Cp), 113.75 (t, Fe–C≡, J_{cp} = 42.45 Hz), 115.82 (s, fc-C≡), 128.00 (s, *m*-Ph, overlap solvent peak), 128.29 (s, *m*-Ph), 128.64, 129.37 (s, *p*-Ph), 132.12, 134.51 (s, *o*-Ph), 138.64–138.94, 143.21–143.38 (m, *ipso*-Ph). ^{31}P NMR (C_6D_6): δ 107.13 (s). MS (ESI): $(M+1)^+$ at m/z 1455. Anal. Calc. for $C_{86}H_{74}Fe_4P_4$: C, 71.00; H, 5.13. Found: C, 71.32; H, 5.26%. M.p.: 214–216 °C. The physical properties of **6** are as follows. ^{1}H NMR (C_6D_6): δ 2.07–2.10 (m, 2H, -PCHCHP-), 2.49 (s, 1H, ≡–H), 2.68–2.71 (m, 2H, -PCHCHP-), 3.77 (t, 2H, fc-Cp, J = 1.5 Hz), 3.80 (t, 2H, fc-Cp, J = 1.8 Hz), 3.85 (t, 2H, fc-Cp, J = 1.5 Hz), 4.00 (t, 2H, fc-Cp, J = 1.2 Hz), 4.11 (t, 2H, fc-Cp, J = 1.8 Hz), 4.18 (t, 2H, fc-Cp, J = 1.5 Hz), 4.28 (s, 5H, CpFe), 4.30 (t, 2H, fc-Cp, J = 1.8 Hz), 4.35 (t, 2H, fc-Cp, J = 1.8 Hz), 6.97–7.02 (m, 6H, Ph), 7.18–7.24 (m, 6H, Ph), 7.31 (t, J = 7.8 Hz, 4H, Ph), 8.07 (t, J = 7.8 Hz, 4H, Ph). ^{13}C NMR (C_6D_6): δ 29.06 (t, -PCH_2CH_2P-, J = 22.1 Hz), 68.04 (s, fc-Cp), 68.49 (s, fc-Cp), 68.97 (s, fc-Cp), 69.64 (s, fc-Cp), 70.14 (s, fc-Cp), 70.60 (s, fc-Cp), 71.16 (s, fc-Cp), 73.25 (s, fc-Cp), 76.90 (s, fc-Cp), 79.49 (s, Cp), 82.65 (s, fc-Cp), 82.95 (s, fc-Cp), 86.93 (s, fc-Cp), 114.75 (t, Fe–C≡, J_{cp} = 42.5 Hz), 115.54 (s, fc–C≡), 128.00 (s, *m*-Ph, overlap solvent peak), 128.29 (s, *m*-Ph), 128.70, 129.39 (s, *p*-Ph), 132.08, 134.49 (s, *o*-Ph), 138.61–138.92, 143.11–143.29 (m, *ipso*-Ph). ^{31}P NMR (C_6D_6): δ 107.25 (s). MS (MALDI-TOF): M^+ at m/z 936. Anal. Calc. for $C_{55}H_{46}Fe_3P_2$: C, 70.54; H, 4.95. Found: C, 70.17; H, 5.15%. M.p.: 168–170 °C. IR (KBr): ν(C≡C) 2108 (w) and 2067 (s) cm^{-1}.

4.5. Preparation of compound 5

A mixture of **12** (50 mg, 0.083 mmol) [27], (η^5-C_5H_5)(dppe)FeCl (180 mg, 0.33 mmol), KPF_6 (100 mg, 0.54 mmol) was stirred in methanol/THF (5:1 30 ml) at room temperature. After stirring for 2 h, potassium *tert*-butoxide (20 mg, 0.2 mmol) was added to the solution. The resulting mixture was stirred for a further 30 min. The solvent was removed under reduced pressure. The crude product was purified by column chromatography on Al_2O_3 (act. III), eluting with hexane/acetone (10:1). The first band was mononuclear Fe^{2+} metallic complex (**7**). The yield of **7** was 4%. The second band was the desired complex (**5**). The yield was 54%. Complex of **5** could be recrystallized from dicholoromethane–hexane to give an orange-red solid compound. The physical properties of **5** are as follows. ^{1}H NMR (C_6D_6): δ 2.08–2.11 (m, 4H, -PCHCHP-), 2.70–2.73 (m, 4H, -PCHCHP-), 3.74 (s, 4H, fc-Cp), 3.77 (s, 4H, fc-Cp), 4.00 (s, 4H, fc-Cp), 4.07 (s, 4H, fc-Cp), 4.14 (s, 4H, fc-Cp), 4.22 (s, 4H, fc-Cp), 4.27 (s, 10H, Cp), 6.97–7.02 (m, 12H, Ph), 7.20–7.23 (m 12H, Ph), 7.30 (t, J = 7.5 Hz, 8H, Ph), 8.07 (br s, 8H, Ph). ^{13}C NMR (C_6D_6): δ 29.10 (t, -PCH_2CH_2P-, J = 22.2 Hz), 68.06 (s, fc-Cp), 68.10 (s, fc-Cp), 68.18 (s, fc-Cp), 69.23 (s, fc-Cp), 69.40 (s, fc-Cp), 71.15 (s, fc-Cp), 76.77 (s, fc-Cp), 79.46 (s, Cp), 83.63 (s, fc-Cp), 85.48 (s, fc-Cp), 114.00 (t, Fe–C≡, J_{cp} = 42.5 Hz), 115.72 (s, fc–C≡), 128.00 (s, *m*-Ph, overlap solvent peak), 128.53 (s, *m*-Ph), 128.66, 129.38 (s, *p*-Ph), 132.13, 134.48 (s, *o*-Ph), 138.62–138.92, 143.18–143.36 (m, *ipso*-Ph). ^{31}P NMR (C_6D_6): δ 107.28 (s). MS (MALDI-TOF): $(M+1)^+$ at m/z 1639. Anal. Calc. for $C_{96}H_{82}Fe_5P_4$: C, 70.36; H, 5.04. Found: C, 70.13; H, 5.41%. M.p.: 130–132 °C. IR (KBr): ν(C≡C) 2067 (s) cm^{-1}. The physical properties of **7** are as follows. ^{1}H NMR (C_6D_6): δ 2.08 (br s, 2H, -PCHCHP-), 2.44 (s, 1H, ≡-H), 2.70 (br s, 2H, -PCHCHP-), 3.74 (br s, 4H, fc-Cp), 3.77 (br s, 2H, fc-Cp), 4.00 (br s, 4H, fc-Cp), 4.07 (br s, 2H, fc-Cp), 4.10 (br s, 4H, fc-Cp), 4.20 (br s, 6H, fc-Cp), 4.24 (br s, 2H, fc-Cp), 4.28 (s, 5H, Cp), 6.95–7.02 (m, 6H, Ph), 7.20–7.24 (m 6H, Ph), 7.30 (t, J = 6.9 Hz, 4H, Ph), 8.06 (br s, 4H, Ph). ^{13}C NMR (C_6D_6): δ 29.05 (t, -PCH_2CH_2P-, J = 22.4 Hz), 68.04 (s, fc-Cp), 68.06 (s, fc-Cp), 68.13 (s, fc-Cp), 68.21 (s, fc-Cp), 68.57 (s, fc-Cp), 69.10 (s, fc-Cp), 69.49 (s, fc-Cp), 69.51 (s, fc-Cp), 70.12 (s, fc-Cp), 70.42 (s, fc-Cp), 71.13 (s, fc-Cp), 73.35 (s, fc-Cp), 76.79 (s, fc-Cp), 79.48 (s, Cp), 82.69 (s, fc-Cp), 83.17 (s, fc-Cp), 83.35 (s, fc-Cp), 85.70 (s, fc-Cp), 85.89 (s, fc-Cp), 114.33 (t, Fe–C≡, J_{cp} = 42.5 Hz), 115.64 (s, fc-C≡), 128.00 (s, *m*-Ph, overlap solvent peak), 128.29 (s, *m*-Ph), 128.70, 129.36 (s, *p*-Ph), 132.11, 134.47 (s, *o*-Ph), 138.64–138.95, 143.12–143.30 (m, *ipso*-Ph). ^{31}P NMR (C_6D_6): δ 107.23 (s). MS (ESI): M^+ at m/z 1120. Anal. Calc. for $C_{65}H_{54}Fe_4P_2$: C, 69.68; H, 4.86. Found: C, 70.14; H, 5.30%. M.p: 70–72 °C. IR (KBr): ν(C≡C) 2106 (w) and 2065 (s) cm^{-1}.

4.6. Preparation of Compounds $[1]^+$ and $[2]^{2+}$

To a solution of **1** (30 mg, 0.022 mmol) or **2** (30 mg, 0.019 mmol) in dichloromethane (1 mL) and benzene (10 mL) was added stoichiometric amount of ferrocenium hexafluorophosphate under N_2 an ice bath. The mixture was stirred for 4 h. The resulting blue precipitates were filtered. The precipitates were recrystallized from dichloromethane/ether to give dark blue desired compound (~80% yield). Anal. Calc. for $C_{76}H_{66}F_6FeP_5Ru_2$ ($[\mathbf{1}]^+$): C, 60.60; H, 4.42. Found: C, 61.19; H, 4.04%. Anal. Calc. for $C_{86}H_{74}F_{12}Fe_2P_6Ru_2$ ($[\mathbf{2}]^{2+}$): C, 56.28; H, 4.06. Found: C, 55.90; H, 4.23%.

4.7. Computational details

Density functional theory calculations at the B3LYP level were performed to obtain the molecular orbitals of **1**–**3**. The basis set used for C, H, P and Fe atoms was 6-31g**, while effective core potentials with a LanL2DZ basis set were employed for Ru. Polarization functions were added for Ru (ζ_d(Ru) = 0.15). All the calculations were made with the use of GAUSSIAN 03. The molecular orbitals were plotted with the Gauss View program.

4.8. Physical methods

^{1}H NMR spectra were run on Varian INOVA-500 MHz spectrometer or INOVA-600 MHz spectrometer. Mass spectra were obtained with a VG-BLOTECH-QUATTRO 5022 system and ESI-LCQ mass spectra were obtained with a Thermo Finnigan spectroscopy. Electrochemical measurements were carried out with a CHI 660B system. Differential pulse voltammetry (DPV) and cyclic voltammetry (CV) were performed with a stationary Pt working electrode. These experiments were carried out with a 1×10^{-3} M solution of dried CH_2Cl_2 containing 0.1 M of (n-C_4H_9)$_4$NPF_6 as supporting electrolyte. The potentials quoted in this work are relative to the Ag/AgCl electrode at 25 °C. Under these conditions, ferrocene shows a reversible one-electron redox wave ($E_{1/2}$ = 0.46 V).

4.9. Structure determination of 2

A yellow-red crystal (0.22 × 0.14 × 0.12 mm) was grown when a layer of hexane was allowed to slowly diffuse into a CH_2Cl_2 solution of **2**. The single crystal X-ray determination of compound **2** was carried out at 120.0(1) K by using a Bruker X8 APEX CCD diffractometer [λ(Mo Kα) = 0.71073 Å], graphite monochromator. Data were collected to a maximum θ value of 27.54°. Of the 35764 reflections collected, there were 7845 independent reflections (R_{int} = 0.0379) with $F^2_o > 2.0\sigma(F^2_o)$. A semi-empirical absorption correction based on azimuthal scans of several reflections was applied. The structures were solved by an expanded Fourier technique. All non-hydrogen atoms were refined anisotropically. Hydrogen atoms were included at ideal distance. Crystal data for **2**: $C_{86}H_{74}Fe_2P_4Ru_2$, M = 1545.17, monoclinic, space

group $P2_1/c$, $a = 9.7846(2)$ Å, $b = 21.8359(5)$ Å, $c = 16.6231(3)$ Å, $\beta = 106.2500(10)^\circ$, $V = 3409.73(12)$ Å^3, $Z = 2$, $D_{calc} = 1.505$ g cm^{-3}, $F(000) = 1580$, μ (Mo Kα) = 0.993 mm^{-1}, Goodness-of-fit = 0.898, $R_1 = 0.0248$ ($I > 2\sigma(I)$), $wR_2 = 0.0485$.

4.10. Structure determination of $\mathbf{4} \cdot C_6H_6$

A yellow-red crystal (0.13 × 0.10 × 0.10 mm) was grown when a layer of ether was allowed to slowly diffuse into a benzene solution of **4**. The single crystal X-ray determination of compound **4** was carried out at 150.0(1) K by using a Bruker X8 APEX CCD diffractometer [λ(Mo Kα) = 0.71073 Å], graphite monochromator. Data were collected to a maximum θ value of 19.85°. Of the 17075 reflections collected, there were 3323 independent reflections ($R_{int} = 0.0839$) with $F^2_o > 2.0\sigma(F^2_o)$. A semi-empirical absorption correction based on azimuthal scans of several reflections was applied. The structures were solved by an expanded Fourier technique. All non-hydrogen atoms were refined anisotropically. Hydrogen atoms were included at ideal distance. Crystal data for $\mathbf{4} \cdot C_6H_6$: $C_{92}H_{80}Fe_4P_4$, $M = 1532.84$, monoclinic, space group $P2_1/n$, $a = 11.6455(6)$ Å, $b = 26.7608(14)$ Å, $c = 11.7964(6)$ Å, $\beta = 96.732(3)^\circ$, $V = 3650.9(3)$ Å^3, $Z = 2$, $D_{calc} = 1.394$ g cm^{-3}, $F(000) = 1592$, μ(Mo Kα) = 0.915 mm^{-1}, Goodness-of-fit = 1.052, $R_1 = 0.0471$ ($I > 2\sigma(I)$), $wR_2 = 0.0957$.

Acknowledgements

We would like to acknowledge Charles P. Casey (University of Wisconsin) for valuable discussions. This work was funded by the National Science Council (NSC95-2113-M-110-014-MY3), Taiwan, ROC, and Department of Chemistry and Center for Nanoscience and Nanotechnology at National Sun Yat-Sen University.

Appendix A. Supplementary material

CCDC 673138 and 673142 contain the supplementary crystallographic data for compounds **2** and $\mathbf{4} \cdot C_6H_6$. These data can be obtained free of charge from The Cambridge Crystallographic Data Centre via www.ccdc.cam.ac.uk/data_request/cif. Supplementary data associated with this article can be found, in the online version, at doi:10.1016/j.jorganchem.2008.12.056.

References

[1] K.D. Demadis, C.M. Hartshorn, T.J. Meyer, Chem. Rev. 101 (2001) 2655.
[2] J.P. Launay, Chem. Soc. Rev. 30 (2001) 386.
[3] B.S. Brunschwig, C. Creutz, N. Sutin, Chem. Soc. Rev. 31 (2002) 168.
[4] A. El-ghayoury, A. Harriman, A. Khatyr, R. Ziessel, Angew. Chem., Int. Ed. Engl. 39 (2000) 185.
[5] A. Harriman, A. Mayeux, A. De Nicola, R. Ziesel, Phys. Chem. Chem. Phys. 4 (2002) 2229.
[6] A. Harriman, A. Khatyr, R. Ziessel, A.C. Benniston, Angew. Chem., Int. Ed. Engl. 39 (2000) 4287.
[7] A. Barbieri, B. Ventura, F. Barigletti, A. De Nicola, M. Quesada, R. Ziessel, Inorg. Chem. 43 (2004) 7359.
[8] J. Hjelm, R.W. Handel, A. Hagfeldt, E.C. Constable, C.E. Housecroft, R.J. Forster, Inorg. Chem. 44 (2005) 1073.
[9] S. Flores-Torres, G.R. Hutchison, L.J. Soltzberg, H.D. Abruña, J. Am. Chem. Soc. 128 (2006) 1513.
[10] Q.Y. Hu, W.X. Lu, H.D. Tang, H.H.Y. Sung, T.B. Wen, I.D. Williams, G.K.L. Wong, Z. Lin, G. Jia, Organometallics 24 (2005) 3966.
[11] M.I. Bruce, P.J. Low, K. Costuas, J.F. Halet, S.P. Best, G.A. Heath, J. Am. Chem. Soc. 122 (2000) 1949.
[12] M.I. Bruce, B.G. Ellis, P.J. Low, B.W. Skelton, A.H. White, Organometallics 22 (2003) 3184.
[13] N.J. Long, C.K. Williams, Angew. Chem., Int. Ed. Engl. 42 (2003) 2586.
[14] N.L. Narvor, L. Toupet, C. Lapinte, J. Am. Chem. Soc. 117 (1995) 7129.
[15] M. Sato, Y. Hayashi, S. Kumakura, N. Shimizu, M. Katada, S. Kawata, Organometallics 15 (1996) 721.
[16] F. Coat, M.A. Guillevic, L. Toupet, F. Paul, C. Lapinte, Organometallics 16 (1997) 5988.
[17] M. Guillemot, L. Toupet, C. Lapinte, Organometallics 17 (1998) 1928.
[18] F. Coat, F. Paul, C. Lapinte, L. Toupet, K. Costuas, J.F. Halet, J. Organomet. Chem. 683 (2003) 368.
[19] M.I. Bruce, P.J. Low, F. Hart, P.A. Humphrey, F. deMontigny, M. Jevric, C. Lapinte, G.J. Perkins, R.L. Roberts, B.W. Skelton, A.H. White, Organometallics 24 (2005) 5241.
[20] M.I. Bruce, K. Costuas, B.G. Ellis, J.F. Halet, P.J. Low, B. Moubaraki, K.S. Murray, N. Oudda, G.J. Perkins, B.W. Skelton, A.H. White, Organometallics 26 (2007) 3735.
[21] M.I. Bruce, K. Costuas, T. Davin, J.F. Halet, K.A. Kramarczuk, P.J. Low, B.K. Nicholson, G.J. Perkins, R.L. Roberts, B.W. Skelton, M.E. Smith, A.H. White, Dalton Trans. (2007) 5387.
[22] R. Dembinski, T. Bartik, B. Bartik, M. Jaeger, J.A. Gladysz, J. Am. Chem. Soc. 122 (2000) 810.
[23] T. Bartik, W. Weng, J.A. Ramsden, S. Szafert, S.B. Falloon, A.M. Arif, J.A. Gladysz, J. Am. Chem. Soc. 120 (1998) 11071.
[24] M. Brady, W. Weng, Y. Zhou, J.W. Seyler, A.J. Amoroso, A.M. Arif, M. Bohme, G. Frenking, J.A. Gladysz, J. Am. Chem. Soc. 119 (1997) 775.
[25] S. Rigaut, C. Olivier, K. Costuas, S. Choua, O.F.J. Massue, P. Turek, J.Y. Saillard, P.H. Dixneuf, D. Touchard, J. Am. Chem. Soc. 128 (2006) 5859.
[26] T.-Y. Dong, K. Chen, M.C. Lin, L. Lee, Organometallics 24 (2005) 4198.
[27] T.-Y. Dong, S.W. Chang, S.F. Lin, M.C. Lin, Y.S. Wen, L. Lee, Organometallics 25 (2006) 2018.
[28] T.-Y. Dong, M.C. Lin, S.W. Chang, C.C. Ho, S.F. Lin, L. Lee, J. Organomet. Chem. 692 (2007) 2324.
[29] M. Sato, H. Shintate, Y. Kawata, M. Sekino, M. Katada, S. Kawata, Organometallics 13 (1994) 1956.
[30] P. Seiler, J.D. Dunitz, Acta Crystallogr. Sect. B 35 (1979) 1068.
[31] T.-Y. Dong, C.H. Huang, C.K. Chang, Y.S. Wen, S.L. Lee, J.A. Chen, W.Y. Yeh, A. Yeh, J. Am. Chem. Soc. 115 (1993) 6357.
[32] N.J. Long, A.J. Martin, R. Vilar, A.J.P. White, D.J. Williams, M. Younus, Organometallics 18 (1999) 4261.
[33] H. Lehmkuh, M. Bellenbaum, J. Grundke, H. Mauermann, C. Kruger, Chem. Ber. 121 (1988) 1719.
[34] F.R. Lemke, D.J. Szalda, R.M. Bullock, J. Am. Chem. Soc. 113 (1991) 8466.
[35] C. Bitcon, M.W. Whiteley, J. Organomet. Chem. 336 (1987) 385.
[36] M.I. Bruce, B.G. Ellis, M. Gaudio, C. Lapinte, G. Melino, F. Paul, B.W. Skelton, M.E. Smith, L. Toupet, A.H. White, J. Chem. Soc., Dalton Trans. 10 (2004) 1601.
[37] M.I. Bruce, B.D. Kelly, B.W. Skelton, A.H. White, J. Organomet. Chem. 640 (2000) 150.
[38] A.B. Antonova, M.I. Bruce, B.G. Ellis, M. Gaudio, P.A. Humphrey, M. Jevric, G. Melino, B.K. Nicholson, G.J. Perkins, B.W. Skelton, B. Stapleton, A.H. White, N.N. Zaitseva, Chem. Commun. (2004) 960.
[39] T.-Y. Dong, C.-C. Schei, T.L. Hsu, S.L. Lee, S.J. Li, Inorg. Chem. 30 (1991) 2457.
[40] R. Prim, F.J. Reinders, J. Am. Chem. Soc. 91 (1969) 4929.
[41] A. Klein, O. Lavastre, J. Fiedler, Organometallics 25 (2006) 635.
[42] N.S. Hush, Inorg. Chem. 8 (1967) 391.
[43] P. Day, Int. Rev. Phys. Chem. 2 (1981) 149.
[44] A.G. Alonso, L.B. Reventós, J. Organomet. Chem. 338 (1988) 249.
[45] M.I. Bruce, B.C. Hall, B.D. Kelly, P.J. Low, B.W. Skelton, A.H. White, J. Chem. Soc., Dalton Trans. (1999) 3719.
[46] M.J. Mays, P.L. Sears, J. Chem. Soc., Dalton Trans. (1973) 1873.